

RESEARCH ARTICLE

Many-scale finite strain computational homogenization via Concentric Interpolation

Oliver Kunc¹ | Felix Fritzen¹

Data Analytics in Engineering, Institute of Applied Mechanics (CE), University of Stuttgart, Stuttgart, Germany

Correspondence

Felix Fritzen, Data Analytics in Engineering, Institute of Applied Mechanics (CE), Pfaffenwaldring 7, 70569 Stuttgart, Germany.
Email: fritzen@mechbau.uni-stuttgart.de

Funding information

Deutsche Forschungsgemeinschaft, Grant/Award Number: project number 390740016, EXC-2075; project number 257987586, grant DFG FR2702/6; project number 406068690, grant DFG FR2702/8

Summary

A method for efficient computational homogenization of hyperelastic materials under finite strains is proposed. Multiple spatial scales are homogenized in a recursive procedure: starting on the smallest scale, few high fidelity FE computations are performed. The resulting fields of deformation gradient fluctuations are processed by a snapshot POD resulting in a reduced basis (RB) model. By means of the computationally efficient RB model, a large set of samples of the homogenized material response is created. This data set serves as the support for the Concentric Interpolation (CI) scheme, interpolating the effective stress and stiffness. Then, the same procedure is invoked on the next larger scale with this CI surrogating the homogenized material law. A three-scale homogenization process is completed within few hours on a standard workstation. The resulting model is evaluated within minutes on a laptop computer in order to generate fourth-scale results. Open source code is provided.

KEYWORDS

computational homogenization, concentric interpolation, Hencky strain, hyperelasticity, multiscale, reduced basis

1 | INTRODUCTION

Homogenization of mechanical properties of solid bodies has caught the attention of researchers for at least 110 years.¹ The ever-increasing interest in efficient two-scale homogenization methods is fueled by the sustainable trend to digitize and automate engineering tasks. This is relevant for both academia and industry.

The subfield of finite strain homogenization comes along with additional difficulties when compared to the infinitesimal strain context: the infinite amount of possible measures of strain and stress, dependencies on finite rotations, and the physical constraint of material self-impenetrability. These are just few examples of increased conceptual and computational complexity as compared to the infinitesimal strain context.

Nonetheless, notable progress in the field of two-scale finite strain homogenization was made recently. An example is the production, experimental investigation, and analytical modeling of fiber-reinforced rubber-like materials.² In other cases, glass fiber-reinforced polymers were efficiently homogenized using a fast Fourier transformation (FFT) scheme.³ A related method was developed for magneto-active materials.⁴

Another interesting movement within the homogenization community is the quest for multi-scale schemes that are capable of bridging more than two scales. For instance, upscaling techniques for three-scale problems involving carbon fibers and epoxy matrices,⁵ layered solids,⁶ or models of porous materials with cracks⁷ were developed. Impressively, the

This is an open access article under the terms of the Creative Commons Attribution License, which permits use, distribution and reproduction in any medium, provided the original work is properly cited.

© 2020 The Authors. *International Journal for Numerical Methods in Engineering* published by John Wiley & Sons Ltd.

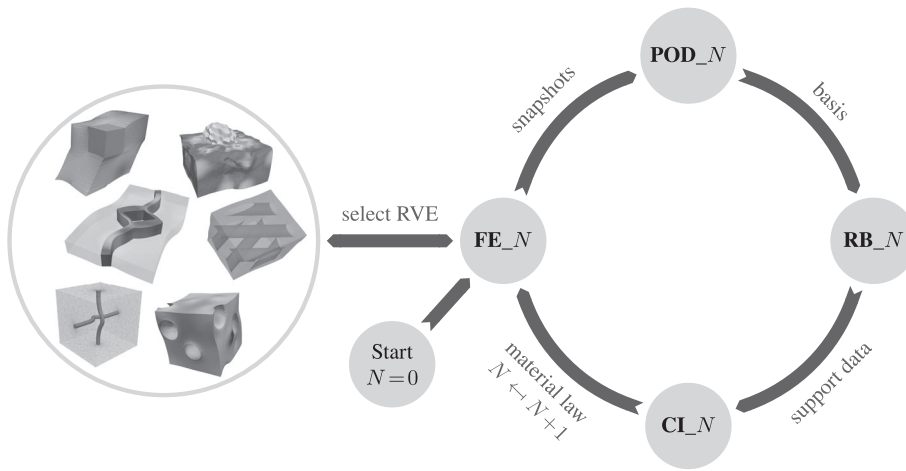


FIGURE 1 Proposed many-scale homogenization scheme for finite strain hyperelasticity. Each complete cycle corresponds to the homogenization of one scale. The procedure is finished after the homogenization of Scales $0, 1, \dots, M - 1$. At this point, the material law $\mathbf{E} \mapsto \mathbf{S}, \mathbb{C}$ on Scale M is efficiently approximated by Concentric Interpolation. Note that the FE method may be replaced by any high-fidelity method, for example FFT. [Colour figure can be viewed at wileyonlinelibrary.com]

mechanical properties of a biological tissue modeled on seven scales were reported.⁸ These and other works exemplify the applicability of homogenization techniques based on multiple, hierarchical separations of scales.

Multiple spatial scales are also studied within scenarios of fractal or self-similar microstructures. Recent examples for this include the analytical homogenization of the elastic properties in the presence of fractal pores⁹ or (without assumed separation of scales) fractal interfaces.^{10,11} Such considerations are motivated, for example, by geology or fracture mechanics.

The present work investigates a computational method for the mechanical homogenization of a large amount of spatial scales—hence the term “many-scale homogenization.” It relies on the presence of exclusively hyperelastic constitutive laws on the smallest scale. There, no assumptions are made on the degree of anisotropy or nonlinearity of the material laws. Also, it allows for an arbitrary amount of material phases—including voids—in any geometric layout, given periodic representative volume elements (RVEs). The latter may or may not differ on each scale. The case of similar RVEs on each scale relates this method to fractal schemes.

The proposed scheme is based on the idea of transitioning from computationally demanding, high fidelity methods to methods compromising some of the accuracy for efficiency. This transition is conducted in a staged manner on each scale, and many scales are processed successively. The scheme is illustrated in Figure 1. Starting on Scale 0, high fidelity finite element (FE) solutions are produced. These are then processed by means of a classical proper orthogonal decomposition (POD) which yields a reduced basis (RB). The latter is, in turn, used to evaluate the homogenized material response at numerous specifically chosen sampling sites within the strain space. This set of data serves as the support of the Concentric Interpolation (CI) scheme, which rapidly approximates the effective constitutive response. With this fast, purely numerical surrogate at hand, the next scale can be homogenized in a similar manner. Eventually, the resulting CI method approximates the material law that is relevant on the engineering Scale M .

The outline is as follows. In Section 2, essential notation is introduced and the multiscale problem as well as the RB scheme are recalled. Section 3 contains the many-scale homogenization algorithm with detailed comments on each step. Numerical examples are presented in Section 4. A summary and additional discussions are given in Section 5.

2 | NOTATION, PROBLEM FORMULATION, AND REDUCED ORDER MODEL

2.1 | Notation

Coordinate-free descriptions of first and second order tensors are denoted by bold letters, for example, \mathbf{X}, \mathbf{F} . The order of a tensor is not related to the capitalization of its representative symbol. Fourth order tensors are written in blackboard bold symbols, for example, \mathbb{C} . Only the set of real numbers \mathbb{R} , its subset $\mathbb{R}_+ = \{x \in \mathbb{R} : x > 0\}$, and the hypersphere $\mathbb{S}^5 = \{\underline{x} \in \mathbb{R}^6 : \|\underline{x}\| = 1\}$ are exceptions to this rule. Real vectors and matrices are denoted by a single and a double underline, for example, $\underline{\underline{x}}$ and $\underline{\underline{F}}$, respectively. Vectors are assumed to be columns, unless transposed, for example, $\underline{\underline{x}}^T$.

In this work, all simulations are conducted in three spatial dimensions. Let $\Omega_0 \subset \mathbb{R}^3$ be the domain of the simply connected physical body in its undeformed state, and $\Omega \subset \mathbb{R}^3$ be the domain occupied by the deformed body. Points within these two sets are referred to as $\mathbf{X} \in \Omega_0$ and $\mathbf{x} \in \Omega$, respectively.

In order to measure the deformation, the deformation gradient $\mathbf{F} = \partial\mathbf{x}/\partial\mathbf{X}$ and the right Cauchy-Green tensor $\mathbf{C} = \mathbf{F}^T\mathbf{F}$ are introduced. The physical impossibility of material self-penetration implies the positiveness of the determinant $J = \det(\mathbf{F}) > 0$, which in turn guarantees the unique existence of the polar decomposition $\mathbf{F} = \mathbf{R}\mathbf{U}$. This yields the rotation tensor \mathbf{R} , with the properties $\det(\mathbf{R}) = 1$ and $\mathbf{R}^T\mathbf{R} = \mathbf{I}$, where \mathbf{I} is the identity tensor, as well as the symmetric positive definite right stretch tensor \mathbf{U} . The Hencky strain $\mathbf{E} = \log(\mathbf{U})$ is of utmost importance to the present work.

Hyperelastic material laws are characterized by elastic energy density functions $W_F(\mathbf{F})$ or $W_C(\mathbf{C})$, respectively, which are equal if their arguments correspond to each other. The \mathbf{F} -energy W_F density gives rise to the first Piola-Kirchhoff stress tensor via differentiation, $\mathbf{P} = \partial W(\mathbf{F})/\partial\mathbf{F}$, while the \mathbf{C} -energy density W_C defines the second Piola-Kirchhoff stress tensor, $\mathbf{S} = \partial W_C(\mathbf{C})/(2\partial\mathbf{C})$. These two stress measures are convertible by the relation $\mathbf{P} = \mathbf{F}\mathbf{S}$. The tangent moduli of the first and of the second Piola-Kirchhoff stresses read $\mathbb{C}_F = \partial^2 W_F(\mathbf{F})/(\partial\mathbf{F})^2$ and $\mathbb{C} = \partial^2 W_C(\mathbf{C})/(4\partial\mathbf{C})^2$, respectively.

For spatial descriptions, the standard Cartesian basis $\mathbf{e}^{(1)}, \mathbf{e}^{(2)}, \mathbf{e}^{(3)}$ is employed. It is orthonormal with respect to the Euclidean inner/dot product and the norm $\|\bullet\|$ induced thereby, that is, $\underline{\mathbf{e}}^{(i)} \cdot \underline{\mathbf{e}}^{(j)} = \underline{\mathbf{e}}^{(i)T} \underline{\mathbf{e}}^{(j)} = \delta_{ij}$ ($i, j = 1, \dots, 3$) holds for the vectorized counterpart of the basis, and δ_{ij} denotes the Kronecker symbol. Components of tensorial quantities are with respect to the tensorial basis $\{\mathbf{e}^{(i_1)} \otimes \dots \otimes \mathbf{e}^{(i_A)}\}_{i_1, \dots, i_A=1,2,3}$, where $A \in \{1,2,4\}$ is the respective tensorial order. Thus, there are natural representations of tensors of first and second order as vectors and matrices respectively, for example, $\mathbf{X} \leftrightarrow \underline{\mathbf{X}} \in \mathbb{R}^3$ or $\mathbf{E} \leftrightarrow \underline{\mathbf{E}} \in \mathbb{R}^{3 \times 3}$. For vectors and matrices of arbitrary dimensions, the Euclidean norm and, respectively, the Frobenius norm are employed.

Two kinds of special tensorial bases are employed. Using a Voigt-like notation, vectorizations of the symmetric second order stress tensor $\mathbf{S} \leftrightarrow \underline{\mathbf{S}} \in \mathbb{R}^6$ are formulated with respect to the basis

$$\begin{aligned} \mathbf{b}^{(1)} &= \mathbf{e}^{(1)} \otimes \mathbf{e}^{(1)}, & \mathbf{b}^{(2)} &= \mathbf{e}^{(2)} \otimes \mathbf{e}^{(2)}, & \mathbf{b}^{(3)} &= \mathbf{e}^{(3)} \otimes \mathbf{e}^{(3)}, \\ \mathbf{b}^{(4)} &= \frac{1}{\sqrt{2}}\mathbf{e}^{(1)} \otimes \mathbf{e}^{(2)}, & \mathbf{b}^{(5)} &= \frac{1}{\sqrt{2}}\mathbf{e}^{(1)} \otimes \mathbf{e}^{(3)}, & \mathbf{b}^{(6)} &= \frac{1}{\sqrt{2}}\mathbf{e}^{(2)} \otimes \mathbf{e}^{(3)}. \end{aligned} \tag{1}$$

Likewise, the matrix variant of the fourth-order stiffness tensor $\mathbb{C} \leftrightarrow \underline{\underline{\mathbf{C}}} \in \mathbb{R}^{6 \times 6}$ with both minor and major symmetry employs the same basis. This basis is compatible with the Euclidean norm, that is, $\|\mathbf{S}\| = \|\underline{\mathbf{S}}\|$. In general, ambiguity of the components of a second order tensor and of its vectorized counterpart is not possible since the former are indexed by two variables, whereas the latter has only one index variable.

Another basis is used with regard to the vectorization of the symmetric Hencky strain $\mathbf{E} \leftrightarrow \underline{\mathbf{E}} \in \mathbb{R}^6$. For this purpose, a family of special bases $\mathcal{Y}_* = \{\underline{\underline{\mathbf{Y}}}^{(1)}, \dots, \underline{\underline{\mathbf{Y}}}^{(5)}, \underline{\underline{\mathbf{Y}}}^{(6)}(J^*)\}$ is introduced:

$$\begin{aligned} \underline{\underline{\mathbf{Y}}}^{(1)} &= \sqrt{\frac{1}{6}} \begin{bmatrix} 2 & 0 & 0 \\ 0 & -1 & 0 \\ 0 & 0 & -1 \end{bmatrix}, & \underline{\underline{\mathbf{Y}}}^{(2)} &= \sqrt{\frac{1}{2}} \begin{bmatrix} 0 & 0 & 0 \\ 0 & 1 & 0 \\ 0 & 0 & -1 \end{bmatrix}, & \underline{\underline{\mathbf{Y}}}^{(3)} &= \sqrt{\frac{1}{2}} \begin{bmatrix} 0 & 1 & 0 \\ 1 & 0 & 0 \\ 0 & 0 & 0 \end{bmatrix}, \\ \underline{\underline{\mathbf{Y}}}^{(4)} &= \sqrt{\frac{1}{2}} \begin{bmatrix} 0 & 0 & 1 \\ 0 & 0 & 0 \\ 1 & 0 & 0 \end{bmatrix}, & \underline{\underline{\mathbf{Y}}}^{(5)} &= \sqrt{\frac{1}{2}} \begin{bmatrix} 0 & 0 & 0 \\ 0 & 0 & 1 \\ 0 & 1 & 0 \end{bmatrix}, & \underline{\underline{\mathbf{Y}}}^{(6)}(J^*) &= \frac{\log(J^*)}{3} \begin{bmatrix} 1 & 0 & 0 \\ 0 & 1 & 0 \\ 0 & 0 & 1 \end{bmatrix}. \end{aligned} \tag{2}$$

These bases are parametrized by the constant dilatational scaling factor,

$$1 < J^* = \text{const}, \tag{3}$$

the meaning of which will be given towards the end of this subsection. The components E_1, \dots, E_6 of $\underline{\mathbf{E}}$ are the coefficients of the \mathcal{Y}_* -representation of $\underline{\mathbf{E}}$,

$$\underline{\mathbf{E}} = \sum_{i=1}^6 E_i \underline{\underline{\mathbf{Y}}}^{(i)} \leftrightarrow \mathbf{E}, \tag{4}$$

where the explicit dependence of the sixth basis element on the scaling factor, $\underline{\underline{Y}}^{(6)} = \underline{\underline{Y}}^{(6)}(J^*)$, is dropped for notational convenience. The equivalence (4) occasionally leads to a slight abuse of notation implying $\underline{\underline{E}} = \underline{\underline{E}}$, which can always be uniquely resolved from the context. Furthermore, the vector $\underline{\underline{E}}$ is decomposed as

$$\underline{\underline{E}} = t\underline{\underline{N}}, \quad t = \|\underline{\underline{E}}\|, \quad \underline{\underline{N}} = \frac{1}{t}\underline{\underline{E}}, \quad (5)$$

where $t \in \mathbb{R}$ and $\underline{\underline{N}} \in \mathbb{S}^5 \subset \mathbb{R}^6$ are called the magnitude and the direction in Hencky strain space, respectively. While the magnitude, t , is one possible scalar measure of strain, the direction in Hencky strain space, $\underline{\underline{N}}$, characterizes the kind of the strain. For instance, $\underline{\underline{N}} = [1, 0, 0, 0, 0, 0]^T \leftrightarrow \underline{\underline{Y}}^{(1)}$ corresponds to isochoric uniaxial extension and $\underline{\underline{N}} = [0, 0, 0, 0, 0, 1]^T \leftrightarrow \underline{\underline{Y}}^{(6)}(J^*)$ corresponds to pure dilatation.

This vectorized notation requires a particular choice of \mathcal{Y}_{J^*} . This choice will always be clear from the context. For simplicity, we only consider Hencky strains with the restriction

$$t \in [0, T_{\max}] \quad (0 < T_{\max} \leq 1). \quad (6)$$

Therefore, the constant dilatational scaling factor, J^* , determines the maximum and the minimum possible determinant of the associated stretch tensor,

$$J = \det(\exp(\pm t Y(J^*))) \in \left[\frac{1}{J^*}, J^* \right]. \quad (7)$$

In general, adaptations to T_{\max} as well as to the normalization of the basis elements $\underline{\underline{Y}}^{(1)}, \dots, \underline{\underline{Y}}^{(5)}$ are admissible. For incompressible materials, it is reasonable to consider only the five-dimensional Hencky strain space spanned by the first five elements of Equation (2) to which the following theory can be easily adapted.¹²

It is important to note that the magnitude, which is the modulus of the vector representation, is generally not the same as the norm of the matrix representation, that is, $t = \|\underline{\underline{E}}\| \neq \|\underline{\underline{E}}\|$ whenever $J^* \neq \exp \sqrt{3}$ and $[0, 0, 0, 0, 0, 1] \underline{\underline{N}} \neq 0$. While the quantity $\|\underline{\underline{E}}\|$ might be of significance in other contexts, we only ever use t instead.

2.2 | Multiscale setting

2.2.1 | Recap of two-scale homogenization

The starting point is the (quasi-)static formulation of the balance equations of linear momentum with respect to the reference configuration Ω_0 , $\text{Div}_{\mathbf{x}}(\mathbf{P}) = \mathbf{B}_{\text{ext}}$, where \mathbf{B}_{ext} denotes the body forces. Complementary, sufficient boundary conditions (BCs) are assumed to be provided and the balance equations of angular momentum hold, $\mathbf{F}^{-1}\mathbf{P} = \mathbf{P}^T\mathbf{F}^{-T}$. The latter will not be addressed in the sequel for the sake of brevity.

In many cases, the domain Ω_0 consists of a very detailed and heterogeneous microstructure that must be resolved for a sufficiently accurate approximation of the solution of the above problem. On the one hand, the microscopic details considered here are of a much smaller characteristic length than that of the overall domain Ω_0 . On the other hand, these microfeatures are still large enough to justify the assumptions of general continuum mechanics.

A well-known method to avoid an excessively fine discretization of the domain Ω_0 (eg, with a FE mesh containing an overly large number of elements) is the method of asymptotic homogenization with assumed separation of scales.¹³ For more details on this well-established procedure, the reader is referred to standard literature.¹⁴

2.2.2 | Multiscale problem

As mentioned in the Introduction, some realistic scenarios make multiple, hierarchical separations of scales desirable. Formally, this is achieved by iteratively stating the assumptions of the classical two-scale procedure. A rigorous derivation and mathematical analysis of this procedure can be found in the seminal works by Bensoussan et al¹⁵ (Chapter 1, Section 8). An informal motivating description of this process is now stated briefly.

Consider a setting in which, after a single scale separation, the emanating RVE of the smaller scale, in turn, exhibits geometric features that are of a much smaller characteristic length than the RVE. Then, another scale separation leads to an even smaller scale with its own RVE and so forth. The total number of scales that is considered within this context is $M + 1$. We count the scales zero-based and in ascending order, that is, Scale 0 denotes the smallest scale and Scale M denotes the engineering scale, for example, the one on which we would like to resolve the original domain. The index $0 \leq N \leq M$ is reserved for reference to an arbitrary scale.

Quantities on Scale N are denoted by N overlines, for example, $\mathbf{F}(\mathbf{X})$ and $\overline{\mathbf{F}}(\overline{\mathbf{X}})$ are the deformation gradients on Scales 0 and 1, respectively. However, if $N > 3$ or if N is not specified, the notation is switched to the corresponding number in parentheses as a superset, for example, $\mathbf{P} = \overline{\overline{\mathbf{P}}}^{(2)}$ or $\mathbb{C}^{(N)}$. For instance, the characteristic lengths of all scales are

$$0 < \underbrace{L}_{\text{Scale 0}} \ll \underbrace{\overline{L}}_{\text{Scale 1}} \ll \underbrace{\overline{\overline{L}}}_{\text{Scale 2}} \ll \dots \ll \underbrace{\overline{\overline{\overline{L}}}}_{\text{Scale } N} \ll \dots \ll \underbrace{\overline{\overline{\overline{\overline{L}}}}}_{\text{Scale } M}. \tag{8}$$

Furthermore, for each separated Scale N ($0 \leq N < M$), there is an RVE which is denoted by $\Omega_0^{(N)}$ in its undeformed configuration. Note that from now on Ω_0 represents the RVE of Scale 0 and $\overline{\Omega}_0^{(M)}$ denotes the whole, original domain without geometric features that are of characteristic length $\leq \overline{\overline{L}}^{(M-1)}$.

The scale separation approach requires compatible kinematic BCs. Multiple such BCs are available and they are characterized by the fact that they fulfill the Hill-Mandel condition. For more details and a discussion of some possible choices, the reader is referred to standard literature.¹⁶ Here, periodic fluctuation BCs for the displacements, $\mathbf{u} = \mathbf{x} - \mathbf{X}^{(N)}$, are chosen. These imply the kinematic scale-coupling relations

$$\langle \mathbf{F} \rangle^{(N)} = \mathbf{F}^{(N+1)}(\mathbf{X}^{(N+1)}), \tag{9}$$

employing the volume averaging operator

$$\langle \bullet \rangle^{(N)} = \frac{1}{|\overline{\Omega}_0^{(N)}|} \int_{\overline{\Omega}_0^{(N)}} \bullet^{(N)}(\mathbf{X}^{(N)}) dV. \tag{10}$$

Moreover, the right-hand side of Equation (9) representing the scale coupling induces a kinematic BC for the problem on Scale N . The complete set of coupled balance equations is stated in the following box:

Scale M :	$\text{Div}_{\mathbf{X}}^{(M)}(\mathbf{P}) = \mathbf{B}_{\text{ext}}^{(M)}$	(BC) (11)
Scale $M - 1$:	$\text{Div}_{\mathbf{X}}^{(M-1)}(\mathbf{P}) = \mathbf{0}$	$\langle \mathbf{F} \rangle^{(M-1)} = \mathbf{F}^{(M)}(\mathbf{X}^{(M)})$ (12)
⋮	⋮	⋮
Scale N :	$\text{Div}_{\mathbf{X}}^{(N)}(\mathbf{P}) = \mathbf{0}$	$\langle \mathbf{F} \rangle^{(N)} = \mathbf{F}^{(N+1)}(\mathbf{X}^{(N+1)})$ (13)
⋮	⋮	⋮
Scale 1:	$\text{Div}_{\overline{\mathbf{X}}}(\overline{\mathbf{P}}) = \mathbf{0}$	$\langle \overline{\mathbf{F}} \rangle = \overline{\overline{\mathbf{F}}}(\overline{\overline{\mathbf{X}}})$ (14)
Scale 0:	$\text{Div}_{\mathbf{X}}(\mathbf{P}) = \mathbf{0}$	$\langle \mathbf{F} \rangle = \overline{\overline{\mathbf{F}}}(\overline{\overline{\mathbf{X}}})$ (15)

The BCs to Scale M may be of any generally admissible type, for example, kinematic, static, or mixed. For each material point $\mathbf{X}^{(N)}$ on Scale N ($0 < N \leq M$), the deformation gradient $\mathbf{F}^{(N)}(\mathbf{X}^{(N)})$ acts as a parameter on Scale $N - 1$ (Chapter 1, Remark 8.5 of Reference 15) representing the corresponding BC. Hence, the problems (12) to (15) need to be solved in a

nested manner. On Scale 0, the material laws of all constituents are assumed to be given explicitly. The ridiculously large computational effort associated with the solution of Equation (11) becomes even more obvious when considering that multiple iterations (e.g., of the Newton method) are required—on each scale. This exponential growth of the algorithmic complexity is long-known and was even literally indicated in the denomination of the FE² method.¹⁷

For notational clarity, the argument of the BC will be omitted in the sequel, $\mathbf{F}(\mathbf{X}) = \mathbf{F}$. It is important to note that the body forces on all but the top scale must equal zero, $\mathbf{B}_{\text{ext}} = \dots = \overline{\mathbf{B}}_{\text{ext}} = \mathbf{B}_{\text{ext}} = \mathbf{0}$, in order for the asymptotic homogenization ansatz to remain valid.

As with the classical two-scale results, the hyperelasticity property is conserved by upscaling, that is the characterizing energy density function on the next scale is the volume average of the respective function on the current scale. The same holds for all additive quantities, but especially *not* for those that are nonlinear with respect to the displacement $\mathbf{u} = \mathbf{x} - \mathbf{X}$. The most relevant statements in this regard are given in the following box:

kinematics:	$\langle \mathbf{F} \rangle = \mathbf{F}$	(16)
	$\langle \mathbf{C} \rangle \neq \mathbf{C} = \mathbf{F}^\top \mathbf{F}$	(17)
energies:	$\langle W_F \rangle = W_F$	(18)
	$\langle W_C \rangle = W_C$	(19)
stresses:	$\langle \mathbf{P} \rangle = \mathbf{P} = \partial W_F / \partial \mathbf{F}$	(20)
	$\langle \mathbf{S} \rangle \neq \mathbf{S} = \partial W_C / (2 \partial \mathbf{C})$	(21)
tangent moduli:	$\langle \mathbb{C}_F \rangle \neq \mathbb{C}_F = \partial^2 W_F / (\partial \mathbf{F})^2$	(22)
	$\langle \mathbb{C} \rangle \neq \mathbb{C} = \partial^2 W_C / (4 \partial \mathbf{C})^2$	(23)

The inequality (17)₁ stems from the quadratic nature of the right Cauchy-Green tensor. From this, the inequality (21)₁ follows, which can be shown by the corresponding form of the Hill-Mandel condition. The non-additivity of stiffness tensors (22)₁ and (23)₁ is adding to the complexity of the computational multi-scale homogenization. Having the stiffness tensor for the subsequent scale accurately represented is required in order to setup reliable multiscale FE simulations with low numbers of nonlinear Newton-Raphson iterations. The classical computational evaluation of $\langle \mathbb{C}_F \rangle$ requires the usage of numerical perturbation of the corresponding stress,¹⁸ or of a computationally very demanding Schur complement technique.¹⁹ The authors have previously introduced a RB method¹² that can efficiently compute the effective stiffness tensor in a two-scale setting. This method will now be briefly introduced and formally generalized to multiple scales. It is crucial to the proposed computational many-scale homogenization method.

2.3 | RB homogenization

The essentials of the RB homogenization method¹² are now summarized in brevity. For more details, the reader is referred to the original open access source. An algorithmic comparison with competing alternative methods can be found in Reference 20. In the following, the transition from Scale N to Scale $N + 1$ is considered, that is $0 \leq N < M$ and $M \geq 1$. In terms of Figure 1, the **RB** _{N} method is now described.

At the core of the RB ansatz is the approximation of the deformation gradient field $\mathbf{F}(\mathbf{X})$. It is additively split into a constant part and a fluctuating part. The constant part, $\mathbf{F}^{(N+1)}$, represents the BC of the respective boundary value problem on Scale N . The fluctuating part vanishes when volume averaged and is a linear combination of the $L^2(\Omega_0)$ -orthonormal RB ansatz functions, $\{\mathbf{B}^{(i)}(\mathbf{X})\}_{i=1, \dots, N_{\text{RB}}} = \mathcal{B}$. For the notation of both the set of basis functions, $\mathcal{B} = \mathcal{B}$, and its size,

$N_{\text{RB}} = N_{\text{RB}}^{(N)}$, we omit the explicit N -dependence. The basis functions are assumed to be given at the moment, their construction is algorithmically described in the next section of this article. Thus, the BC and the vector of RB coefficients, $\underline{\xi} = \underline{\xi}^{(N)} \in \mathbb{R}^{N_{\text{RB}}}$, are included as parameters in the RB approximation

$$\mathbf{F}(\mathbf{X}) \approx \mathbf{F}_{\text{RB}}^{(N)}(\mathbf{X}; \mathbf{F}, \underline{\xi}) = \mathbf{F}^{(N+1)} + \sum_{i=1}^{N_{\text{RB}}} \xi_i \mathbf{B}^{(N)}(\mathbf{X}). \quad (24)$$

As a fundamental principle of mechanics, the energy integral is sought to be minimized,

$$\left\langle W_{\text{F}}^{(N)} \left(\mathbf{F}_{\text{RB}}^{(N)} \left(\mathbf{X}; \mathbf{F}, \underline{\xi} \right) \right) \right\rangle \rightarrow \min_{\underline{\xi} \in \mathbb{R}^{N_{\text{RB}}}} ! \quad (25)$$

From this and from the fact that the ansatz (24) is a low-dimensional approximation within the space of all deformation gradients, it follows (Section 2.3 of Reference 12) that

$$\left\langle W_{\text{F}}^{(N)} \left(\mathbf{F}_{\text{RB}}^{(N)} \left(\mathbf{X}; \mathbf{F}, \underline{\xi} \right) \right) \right\rangle \geq W_{\text{F}}^{(N+1)}(\mathbf{F}), \quad (26)$$

meaning that the solution to Equation (25) realizes the best approximation of the true effective energy density.

Once sufficient convergence (see Equation (28) of Reference 12) of Equation (25) is achieved, the RB approximations of the effective first Piola-Kirchhoff stress tensor $\mathbf{P}_{\text{RB}}^{(N+1)}$ and of its corresponding tangent modulus $\mathbb{C}_{\text{F;RB}}^{(N+1)}$ are readily available, cf. Appendix B of Reference 12. Next, these are converted to their equivalents with respect to the right Cauchy-Green tensor,

$$\mathbf{S}_{\text{RB}}^{(N+1)} = \mathbf{F}^{(N+1)-1} \mathbf{P}_{\text{RB}}^{(N+1)} \quad (27)$$

$$\left(\mathbb{C}_{\text{RB}}^{(N+1)} \right)_{ijkl} = \left(\sum_{a,b=1}^3 \left(\mathbf{F}^{(N+1)-1} \right)_{ia} \left(\mathbb{C}_{\text{F;RB}}^{(N+1)} \right)_{ajbl} \left(\mathbf{F}^{(N+1)-T} \right)_{bk} \right) - \left(\mathbb{C}^{-1} \right)_{ik} \left(\mathbf{S}_{\text{RB}}^{(N+1)} \right)_{lj} \quad (i, j, k, l = 1, 2, 3). \quad (28)$$

The formulation with respect to the second Piola-Kirchhoff stress and its tangent modulus is widely used for the implementation of material routines, for example, in the context of the FEM. Thus, this RB method may be easily wrapped for the employment in such simulation software. This holds true even for commercial products as long as a user-defined material interface is provided, which usually is the case. The computational effort for a single evaluation of the stress in Equation (27) is significantly reduced compared to the FEM as the solution of the minimization task (25) depends on just N_{RB} DOF. Usually, N_{RB} is on the order of 20-100. Apart from this speed-up, a good approximation of the tangent modulus is given by Equation (28).

However, the volume averaging operator requires integration over the RVE Ω_0 , cf. (10). This operator is invoked multiple times per iteration of the minimization task (26). Thus, although the number of DOF is drastically reduced in comparison to the FEM, the original spatial complexity is still present by the number of integration points. For this reason, the unmodified RB method as described above is not suitable for online application in many-scale simulations. Several opportunities for further speed-up are discussed in the original paper.¹² For now, we settle with the moderate speed-up factor of 10-100 with respect to the FEM (not accounting for the setup phase of the RB), as the RB method is part of the offline phase of the proposed many-scale scheme.

3 | COMPUTATIONAL HOMOGENIZATION VIA CI

The CI method was recently introduced by the authors²¹ in its general form. Previously, it was employed in the RNEXP method²² in an ad-hoc manner. It serves as another major building block for the proposed many-scale computational homogenization scheme. In terms of Figure 1, the RB method efficiently provides some evaluations of the homogenized material law. These data are used as supporting data for the subsequent CI method. While the RB method as treated in this

context is based on the fundamental physical principle of energy minimization, the CI method is a purely mathematical means of function approximation. However, its particular design is specialized to the characteristics of material laws and enables very efficient numerical treatment of material data, accounting for the usually rather sparse availability of the latter.

The C/C++ implementation of the CI scheme employed in this study is provided as open source code.²³ The repository includes an example in which the hyperelastic material law ETM from Section 4.1 is interpolated. For this, compile `demo_largeststrain` in the subfolder `examples`, and then execute the corresponding binary in the `bin` folder.

3.1 | Basic scheme

The CI method is a specialization of the established general kernel interpolation method. It is standard²⁴ that the approximation \tilde{f} of a scalar function $f: \mathbb{R} \rightarrow \mathbb{R}$ by N^{supp} symmetric positive definite kernel functions $k_i: \mathbb{R} \rightarrow \mathbb{R}_+$ ($i = 1, \dots, N^{\text{supp}}$) takes the form

$$f(x) \approx \tilde{f}(x) = \underline{p}^T \underline{\underline{K}}^{-1} \underline{k}(x). \quad (29)$$

The kernel functions $k_i(x) = k(x_i, x)$ are identical up to the locations of the support points, $x_1, \dots, x_{N^{\text{supp}}}$. These functions constitute the components of the kernel vector $\underline{k}(x)$, whereas the kernel matrix $\underline{\underline{K}} \in \mathbb{R}^{N^{\text{supp}} \times N^{\text{supp}}}$ is composed of the values $K_{ij} = k_i(x_j) = K_{ji}$. The function values at the kernel centers define the components of the vector \underline{p} , that is, $p_i = f(x_i)$.

In the multivariate case, $f: \mathbb{R}^D \rightarrow \mathbb{R}$, $D \geq 1$, radial basis functions of the kind $k(\underline{x}, \underline{y}) = \Phi(\|\underline{x} - \underline{y}\|)$, with $\Phi: \mathbb{R}_+ \rightarrow \mathbb{R}_+$, are common for use as kernel functions. The restriction to the hypersphere, $f: \mathbb{S}^{D-1} \rightarrow \mathbb{R}$, $\mathbb{S}^{D-1} = \{\underline{x} \in \mathbb{R}^D : \|\underline{x}\| = 1\}$, by substituting the geodesic (i.e., angular) distance function, $\text{acos}(\underline{x} \cdot \underline{y})$, for the argument in Φ is known as spherical basis function ansatz (§6 of Reference 25). A popular choice for kernel functions is the Gaussian kernel, which then takes the form

$$k(\underline{x}, \underline{y}) = \exp(-\gamma \text{acos}^2(\underline{x} \cdot \underline{y})). \quad (30)$$

In the present work, attention is restricted to this kernel function and investigations of possible alternatives is not within the current scope. Since the kernel centers are points on a unit hypersphere, they are from now on denoted support directions, and accordingly their number is $N_{\text{dir}}^{\text{supp}}$.

The CI method is an extension of this spherical interpolation on the hypersphere \mathbb{S}^{D-1} to the surrounding Euclidean space \mathbb{R}^D . This is achieved by first splitting the argument $\underline{x} \in \mathbb{R}^D$ into its magnitude t and its direction \underline{N} ,

$$\underline{x} = t \underline{N} \quad t = \|\underline{x}\| \quad \underline{N} = \frac{1}{t} \underline{x}. \quad (31)$$

Then, the spherical interpolation ansatz from above, classically acting exclusively on $\underline{N} \in \mathbb{S}^{D-1}$, is complemented by the introduction of a dependence of the vector of function values on the magnitude $t \in \mathbb{R}_+$,

$$f(\underline{x}) \approx \tilde{f}(t, \underline{N}) = \begin{cases} \underline{p}(t)^T \underline{\underline{K}}^{-1} \underline{k}(\underline{N}) & \text{if } t \neq 0 \\ 0 & \text{if } t = 0 \end{cases}. \quad (32)$$

Here, it is assumed without loss of generality that $f(\underline{0}) = 0$, which can always be ensured by shifting the function values. Accordingly, the components of the function value vector $\underline{p}(t), p_i(t): \mathbb{R}_+ \rightarrow \mathbb{R}$, are chosen with the property $p_i(0) = 0$. More precisely, these functions are defined as piecewise linear polynomials and the same set of support magnitudes $0 < t_1 < \dots < t_{N_{\text{mag}}^{\text{supp}}} = 1$ is chosen for all $i = 1, \dots, N_{\text{dir}}^{\text{supp}}$. Hence, there is a distinct one-dimensional approximation of the function values along each of the $N_{\text{dir}}^{\text{supp}}$ supporting directions.

The total number of function values necessary for the setup of the CI scheme is $N_{\text{dir}}^{\text{supp}} N_{\text{mag}}^{\text{supp}}$ and can be adjusted according to the properties of the target function f . Also, the placement of the magnitude support points $t_1, \dots, t_{N_{\text{mag}}^{\text{supp}}}$ may be adapted in a problem specific manner. However, the choice of the support directions $\underline{N}^{(1)}, \dots, \underline{N}^{(N_{\text{dir}}^{\text{supp}})}$ is strongly constrained by the choice of identical kernel functions of the kind (30) for each of the components of the kernel vector $\underline{k}(\underline{N})$, that is, all kernel functions share the same kernel parameter γ . Thus, the directions are sought to be asymptotically uniformly distributed.²¹

3.2 | Efficient implementation

The approximant \tilde{f} from (32) can be highly efficiently implemented: by means of dedicated matrix-vector representations of the involved quantities, the inverse kernel matrix, $\underline{\underline{K}}^{-1}$, can be multiplied with static data during the setup phase. Then, each evaluation of $\tilde{f}(t, \underline{N})$ reduces to the evaluation of the radial interpolation vector, $\underline{p}(t)$, the kernel vector, $\underline{k}(\underline{N})$, and some matrix-vector multiplications.

For the sake of simplicity, this is now exemplified assuming the radial interpolation vector, $\underline{p}(t) \in \mathbb{R}^{N_{\text{dir}}^{\text{supp}}}$, is linear on the whole domain \mathbb{R}_+ , that is, not just piecewise. Then, it has the discrete representation

$$\underline{p}(t) = \begin{bmatrix} a_1 & b_1 \\ a_2 & b_2 \\ \vdots & \vdots \\ a_{N_{\text{dir}}^{\text{supp}}} & b_{N_{\text{dir}}^{\text{supp}}} \end{bmatrix} \begin{bmatrix} t \\ 1 \end{bmatrix}. \quad (33)$$

Here, the components a_i and b_i are the polynomial coefficients of the component $p_i = a_i t + b_i$, $i = 1, \dots, N_{\text{dir}}^{\text{supp}}$. Substitution into Equation (32) yields

$$\tilde{f}(t, \underline{N}) = \begin{bmatrix} t & 1 \end{bmatrix} \underbrace{\begin{bmatrix} a_1 & a_2 & \dots & a_{N_{\text{dir}}^{\text{supp}}} \\ b_1 & b_2 & \dots & b_{N_{\text{dir}}^{\text{supp}}} \end{bmatrix}}_{\text{constant}} \underline{\underline{K}}^{-1} \underline{k}(\underline{N}). \quad (34)$$

In the actual implementation with piecewise linearity of \underline{p} , the polynomial coefficients are stored in $N_{\text{mag}}^{\text{supp}}$ sets, each of which is multiplied with the inverse kernel matrix in analog to Equation (34) during the setup phase.

3.3 | Concentric Interpolation of material laws

FE software oftentimes provides an interface to user-defined material routines. In finite strain hyperelasticity, material laws are usually defined with respect to rotationally invariant kinematic descriptors, such as \underline{U} or $\underline{C} = \underline{U}^2$. However, as the authors previously emphasized,¹² it is advantageous for a number of reasons to sample mechanical response functions on the space of Hencky strains, $\underline{E} = \log(\underline{U})$. Additionally, the space of Hencky strains is isomorphic to \mathbb{R}^6 , cf. (4), allowing for the application of CI, $\tilde{f} : \mathbb{R}^6 \rightarrow \mathbb{R}$. In principle, the form of the interpolant, cf. Equation (32), is suitable for approximating the hyperelastic energy density function, $W_{\underline{C}} = W_{\underline{C}}(\exp(2\underline{E}))$. Furthermore, if sufficiently smooth one-dimensional radial interpolation functions, p_i , were used instead of piecewise linear polynomials, the stress, \underline{S} , and its tangent modulus, \underline{C} , could be computed by means of differentiation. However, differentiation comes along with significant increases of the number of linear operations (Section 5.3 of Reference 22). Moreover, the involved derivatives of the matrix exponential and of the matrix logarithm are highly non-trivial to implement. A different approach is pursued here for these reasons.

Instead of interpolating the energy density function, the second Piola-Kirchhoff stress, $\underline{S} \leftrightarrow \underline{S} \in \mathbb{R}^6$, and its tangent modulus, $\underline{C} \leftrightarrow \underline{C} \in \mathbb{R}^{21}$ are directly interpolated over the space of Hencky strains, $\underline{E} \leftrightarrow \underline{E} \in \mathbb{R}^6$. It is important to recall that the basis (1) is employed for the stress and the stiffness, while the Hencky strain is formulated with respect to the

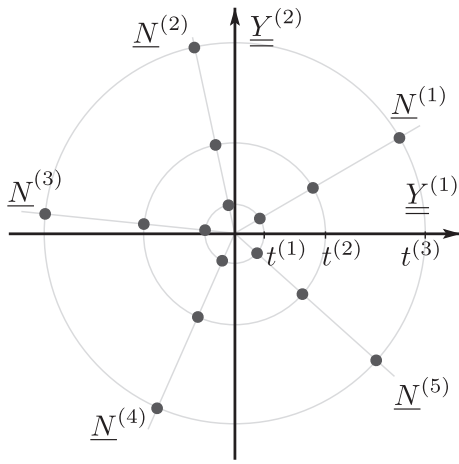


FIGURE 2 Sketch of concentric sampling of the Hencky strain space. For visualization purposes, only two of the six coordinate axes of \mathcal{Y}_{J^*} are considered. N_{mag} samples are placed along N_{dir} approximately uniformly distributed directions. The former characterize the load magnitudes, the latter correspond to the type of the load [Colour figure can be viewed at wileyonlinelibrary.com]

basis (2). The CI ansatz is modified into

$$\begin{bmatrix} \underline{S}(\underline{E}) \\ \underline{C}(\underline{E}) \end{bmatrix} \approx \tilde{f}(\underline{t}, \underline{N}) = \left[\underline{p}^{(1)}(\underline{t}), \dots, \underline{p}^{(27)}(\underline{t}) \right]^T \underline{K}^{-1} \underline{k}(\underline{N}) \in \mathbb{R}^{6+21}, \quad (35)$$

meaning that all 27 components (6 for the stress and 21 for the stiffness) are interpolated separately but simultaneously: the respective functional data is independently interpolated by the $N_{\text{dir}}^{\text{supp}}$ distinct components of the vector $\underline{p}^{(i)}(\underline{t})$ ($i = 1, \dots, 27$). The magnitude, \underline{t} , and the direction, \underline{N} , of the query Hencky strain, \underline{E} , are computed as defined in Equation (5).

By interpolating the components of the stress and of the stiffness separately, their consistency is generally lost. Thus, a possibly negative effect on the convergence behavior of Newton-Raphson is to be expected and will be investigated in the numeric section of this article. One way to principally attenuate this drawback could be to incorporate FFT-based homogenization schemes^{26,27} on the lower scales as such schemes are generally less sensitive to the tangent modulus. Alternatively, automatic differentiation²⁸ (AD) of the energy density function W_C could possibly be employed for the evaluation of derivatives, similar to previous works.²²

3.4 | Concentric Sampling of material laws

The CI method crucially depends on the concentric sampling (CS) method. The CS algorithm employed in this work is a slight modification of the original (see Algorithm 1 of Reference 12) and is essentially described by the following construction of Hencky strains, cf. Equations (4), (5):

$$\underline{E}^{(m,n)} \leftrightarrow \underline{\underline{E}}^{(m,n)} = \underline{t}_m \sum_{i=1}^6 N_i^{(n)} \underline{\underline{Y}}^{(i)} \quad (m = 1, \dots, N_{\text{mag}}, n = 1, \dots, N_{\text{dir}}). \quad (36)$$

Here, a Hencky strain basis $\underline{\underline{Y}}^{(i)} \in \mathcal{Y}_{J^*}$ ($i = 1, \dots, 6$) with fixed scaling factor J^* is considered. Furthermore, a set of asymptotically uniformly distributed points on the five-dimensional unit hypersphere, $\underline{\underline{N}}^{(n)} \in \mathbb{S}^5 \subset \mathbb{R}^6 \sim \text{span}(\mathcal{Y}_{J^*})$, $n = 1, \dots, N_{\text{dir}}$, is assumed to be provided. Such point sets may be constructed, for example, by means of the `MinimumEnergyPoints` open source Matlab/Octave code provided by the authors.²⁹ These hyperspherical points are interpreted as directions within the Hencky strain space along which samples are placed. The distribution of the samples along each direction is given by the set of sampling magnitudes, $0 < t_1, \dots, t_{N_{\text{mag}}} = 1$. A visualization in two dimensions is provided in Figure 2, where $N_{\text{dir}} = 5$ and $N_{\text{mag}} = 3$.

When the Hencky strains obtained through CS are utilized as support points for the CI method, the nomenclature $N_{\text{dir}} = N_{\text{dir}}^{\text{supp}}$ and $N_{\text{mag}} = N_{\text{mag}}^{\text{supp}}$ is adopted. On the other hand, if the CS points are evaluation points of the CI scheme, this is denoted by $N_{\text{dir}} = N_{\text{dir}}^{\text{eval}}$ and $N_{\text{mag}} = N_{\text{mag}}^{\text{eval}}$. Accordingly, when the resulting stretch tensors, $\exp \underline{E}^{(m,n)}$, are applied

as BCs to the boundary value problems (12) to (15), this is again denoted by $N_{\text{dir}} = N_{\text{dir}}^{\text{eval}}$ and $N_{\text{mag}} = N_{\text{mag}}^{\text{eval}}$, regardless of the employed solution method, FE, or the RB.

By means of this sampling approach, *representative* and *unbiased* sampling of the Hencky strain space and, thus, after exponentiation, of the *physically meaningful* part of the space of stretch tensors is realized:

- *Representative* means that the sampled space is covered in a manner that is dense with respect to a certain metric, given a limited number of discrete sampling points. In the case of material laws, the metric is the angular distance between different load directions, $\text{acos}(\underline{N}^{(i)} \cdot \underline{N}^{(j)})$. Sampling the directions in an approximately uniform manner ensures that the resolution of the anisotropy of the present material law can be adjusted.
- *Unbiased* means that the resolution by which different regions of the domain are covered is either constant or deliberately adapted. The radial density of the samples in the CS method may be adjusted according to expected features of the present material law. For instance, if a significant change of the material response is expected at certain load magnitude, for example, a transition from linear to nonlinear behavior, then a neighborhood of this critical point may be resolved more thoroughly.
- *Physically meaningful*, in the context of sampling of kinematic quantities, such as the stretch tensor $\mathbf{U} = \exp(\mathbf{E})$, means that the sampling domain is confined in such a way that all contained points correspond to realistic deformations that might actually occur in real-world problems. This is one of the main advantages of the CS method in contrast to classical approaches that directly sample the space of stretch tensors, right Cauchy-Green tensors, or deformation gradients with uniform Cartesian grids.^{30,31} Such grid-based sampling methods are unable to keep the determinant $J = \det(\mathbf{U})$ within realistic bounds (eg, $1 \pm \varepsilon$ in the quasi-incompressible case) while also exploring isochoric regions of the respective kinematic state spaces to their whole physically meaningful extent, for example, more than 100% strain for rubber-like materials.

3.5 | Many-scale homogenization: Overall algorithm

The proposed method is a many-scale solution to the multi-scale problem: it is emphasized that not just more than one scale but actually numerous scales are transitioned. As indicated in Figure 1, the lowest M scales of the general multi-scale problem, cf. Equations (12) to (15), are homogenized in a recursive manner. Then, the resulting numerical surrogate of the homogenized material law can be applied on the engineering scale. The complete procedure is formally stated in Algorithm 1. A thorough step-by-step description is given in the following. We omit the scale index N on top of some quantities for the sake of enhanced readability.

Algorithm 1. Many-scale homogenization for finite strain hyperelasticity

input number M of scales to be homogenized; set of RVE's $\left\{ \Omega_0^{(N)} \right\}_{N=0, \dots, M-1}$; scalar parameters for the sub-algorithms 2, 3, 4, 5

for $N = 0, \dots, M - 1$ **do** ▷ loop Scales

call Algorithm 2: $\mathbf{FE}_N \left(\Omega_0^{(N)}, N_{\text{dir}}^{\text{eval}}, N_{\text{mag}}^{\text{eval}}, J^*, T_{\text{max}} \right) \rightarrow \mathcal{S}$ ▷ generate snapshots

call Algorithm 3: $\mathbf{POD}_N(\mathcal{S}, N_{\text{RB}}) \rightarrow \mathcal{B}$ ▷ determine RB

call Algorithm 4: $\mathbf{RB}_N(\mathcal{B}, N_{\text{dir}}^{\text{eval}}, N_{\text{mag}}^{\text{eval}}, J^*, T_{\text{max}}) \rightarrow \mathcal{D}$ ▷ generate CI support data

setup $\mathbf{CI}_N(\mathcal{D}, N_{\text{dir}}^{\text{supp}}, N_{\text{mag}}^{\text{supp}}, \gamma)$ ▷ homogenized material law

if $N < M - 1$ **then**

set \mathbf{CI}_N as material law in (one phase of) the RVE $\Omega_0^{(N+1)}$ of the next scale ▷ use Algorithm~5

else

set \mathbf{CI}_N as material law in (one phase of) the engineering Scale~ M ▷ use Algorithm~5

end if

end for

For the sake of brevity, the scaling parameter J^* is fixed throughout the whole algorithm, that is, across all scales, which conforms with the numerical experiments of the next section. If the query Hencky strain was ever out of the sampling range defined by T_{\max} and J^* , the CI routine would still return a result by means of extrapolation.

3.5.1 | FE simulations

On Scale N , the FE method is invoked by a call to Algorithm 2 which is denoted **FE_N**. Kinematic periodic fluctuation BCs, defined in terms of stretch tensors corresponding to Hencky strains (36) on Scale $N + 1$, are prescribed to the RVE $\Omega_0^{(N)}$. These BCs are chosen by means of the CS method of Section 3.4. In view of limited computational resources the parameters $N_{\text{dir}}^{\text{eval}}$ and $N_{\text{mag}}^{\text{eval}}$ are chosen in order to balance data availability (and thereby accuracy) and computational cost. A discussion of their physical interpretation is included in Section 3.4. Moreover, the choice of these parameters depends on the complexity of FE simulations, which is strongly influenced by the mesh of $\Omega_0^{(N)}$, the local material laws, the stability of the element formulation, and the efficiency of the FE implementation. Empirically speaking, $N_{\text{dir}}^{\text{eval}} = 100$ and $N_{\text{mag}}^{\text{eval}} = 10$ are practical starting points for the present study.

Algorithm 2. Finite Element sub-routine **FE_N**

input RVE $\Omega_0^{(N)}$; number of load directions $N_{\text{dir}}^{\text{eval}}$; number of load magnitudes $N_{\text{mag}}^{\text{eval}}$; scaling factor J^* of Hencky strain basis; maximum load magnitude T_{\max} ; load directions $\{\underline{N}^{(n)}\}_{n=1, \dots, N_{\text{dir}}^{\text{eval}}} \subset \mathbb{S}^6$; load magnitudes $\{t_m\}_{m=1, \dots, N_{\text{mag}}^{\text{eval}}} \subset [0, T_{\max}]$

initialize snapshot list $S = \{\}$

for $n = 1, \dots, N_{\text{dir}}^{\text{eval}}$ **do** ▷ loop directions

for $m = 1, \dots, N_{\text{mag}}^{\text{eval}}$ **do** ▷ loop magnitudes

$\underline{U}^{(N+1)} = \exp\left(t_m \sum_{i=1}^6 N_i^{(n)} \underline{Y}^{(i)}\right)$ ▷ boundary condition
 $\underline{Y}^{(i)} \in \mathcal{Y}_{J^*}$

 try to solve boundary value problem (13) on $\Omega_0^{(N)}$ with boundary condition $\underline{U}^{(N+1)}$ using FEM

if convergence **then**

 subtract homogeneous deformation from local field, $\tilde{\underline{F}}^{(N)}(\underline{X}) = \underline{F}^{(N)}(\underline{X}) - \underline{U}^{(N+1)}$ ▷ fluctuation snapshot

 include fluctuation snapshot in list, $S \leftarrow S \cup \left\{ \tilde{\underline{F}}^{(N)}(\underline{X}) \right\}$

end if

end for

end for

output deformation gradient fluctuation snapshots S with $|S| = N_{\text{snap}}$ ($N_{\text{snap}} \leq N_{\text{dir}}^{\text{eval}} N_{\text{mag}}^{\text{eval}}$)

It is important to note the order in which the BCs are applied: the FE method generally converges quicker if only the load magnitude, t , is incremented between load steps and the kind of the load, that is its direction \underline{N} with respect to the Hencky strain representation, is kept constant. Furthermore, very simple parallelization of the overall workload is possible by running multiple instances of the same program with different sets of loading directions. For instance, if the number of available compute threads is 10 and $N_{\text{dir}}^{\text{eval}} = 100$, one might run 10 instances in parallel, each applying 10 different load directions successively.

The Newton iterations of the FEM are stopped when the maximum nodal residual is below $10^{-5} \text{MPa} \cdot L^2$ (where L is the side length of the cubic RVE) or if its ratio to the maximum reaction force is below 10^{-3} . In the present study, the same stopping FE criterion is employed on all scales. This is in contrast to other works³² that eased the stopping criterion on larger scales.

Usual convergence issues are expected at some evaluation directions above few critical load magnitudes (see Section 3.2.5 of Reference 30). In practice, certain states of (large) deformations simply cannot be reached by a given

FE model. This effect depends on the maximum magnitude T_{\max} , the properties of the mesh, the element stabilization method, the material laws employed at the current Scale N , the scaling parameter J^* , among other factors. Therefore, the number of available solutions is usually lower than the number of BCs provided by CS. In order to conservatively assess the practicality of the proposed method, no FE stabilization method is employed in the present study.

The converged resulting fields of deformation gradients are post-processed by pointwise subtraction of the prescribed homogeneous deformation. Thus, the set S of deformation gradient fluctuation fields is computed, denoted snapshots, and returned to the main routine.

3.5.2 | Proper Orthogonal Decomposition

The set of deformation gradient fluctuation snapshots, S , is processed by the POD Algorithm 3, which is dubbed **POD_N**. Snapshot POD methods of this kind have been successfully applied before.³³

Algorithm 3. Proper Orthogonal Decomposition sub-routine **POD_N**

input snapshot list S with $|S| = N_{\text{snap}}$; Reduced Basis size N_{RB} with $1 \leq N_{\text{RB}} \leq N_{\text{snap}}$; RVE domain $\Omega_0^{(N)}$ (implicit)

for $i = 1, \dots, N_{\text{snap}}$ **do**

for $j = i, \dots, N_{\text{snap}}$ **do**

$\Gamma_{ij}^{(N)} = \langle \tilde{\mathbf{F}}^{(i)}, \tilde{\mathbf{F}}^{(j)} \rangle = \Gamma_{ji}^{(N)}$ ▷ correlation matrix

end for

end for

solve eigenvalue problem of $\underline{\Gamma} \in \mathbb{R}^{N_{\text{snap}} \times N_{\text{snap}}}$ ▷ eigendecomposition

 → eigenvalues $\kappa_1 > \dots > \kappa_{N_{\text{snap}}} > 0$, corresponding eigenvectors $\underline{V}^{(1)}, \dots, \underline{V}^{(N_{\text{snap}})} \in \mathbb{R}^{N_{\text{snap}}}$

for $i = 1, \dots, N_{\text{RB}}$ **do** ▷ truncation

$\mathbf{B}^{(i)}(\mathbf{X}) = \sum_{j=1}^{N_{\text{snap}}} \frac{1}{\sqrt{\kappa_i}} V_j^{(i)} \tilde{\mathbf{F}}^{(j)}(\mathbf{X})$ ▷ normalized Reduced Basis

end for

output $\mathcal{B} = \left\{ \mathbf{B}^{(i)}(\mathbf{X}) \right\}_{i=1, \dots, N_{\text{RB}}}$

A popular way of deciding when to truncate the emanating set of basis functions, that is, how large to choose the number $N_{\text{RB}} = |\mathcal{B}|$ of basis functions, is to employ the Eckart-Young-Mirsky theorem. By this, the resulting projection error can be controlled based on the eigenvalues of the correlation matrix. However, the authors have experienced¹² a deteriorating effect in terms of the stress approximation error with N_{RB} values greater than a certain optimum. This effect is interpreted as an artifact stemming from spurious displacement patterns (for instance strongly oscillating fields) mainly located at the interface of high contrast materials. The severity of this effect has yet to be investigated systematically.

For the moment, we settle with the empirically determined¹² number of $N_{\text{RB}} = 30$ basis elements, which appears to give reasonably good approximation accuracy of both the energy density and the stresses. Also, the resulting speed-up compared with the FE method remains significant. The truncated basis \mathcal{B} is returned to the main algorithm.

3.5.3 | RB simulations

Just as the FEM, the RB model is evaluated at kinematic BCs corresponding to Hencky strains that result from CS. But in contrast to the FE model, the numbers $N_{\text{dir}}^{\text{eval}}$ and $N_{\text{mag}}^{\text{eval}}$ are chosen significantly larger for the call of the **RB_N** (Algorithm 4).

As a rule of thumb, the number of BCs, $N_{\text{dir}}^{\text{eval}} N_{\text{mag}}^{\text{eval}}$, applied to **RB** $_N$ can be greater than that of **FE** $_N$ by the same factor as the speed-up of the RB with respect to the FEM. This way, the computational work load associated with these two stages of the overall homogenization process is comparable. Positive experiences were obtained by increasing $N_{\text{dir}}^{\text{eval}}$ by a factor of 5 and $N_{\text{mag}}^{\text{eval}}$ by a factor of 2, corresponding to a speed-up factor of approximately 10.

The choice of these parameters strongly depends on the size of the RB, N_{RB} . On the one hand, a smaller basis is advantageous in that a greater number of BCs can be applied, that is a greater sampling resolution can be achieved. On the other hand, the quality of this sampling data is increased by a larger basis. It is a complex task to choose all parameters (of the RB but also of the overall method) in an optimal way.

Importantly, the robustness of the RB method is greatly increased in contrast to the FEM. Hence, the maximum magnitude T_{max} may be chosen much larger for the RB than for the FE model. However, one should keep in mind that the reliability of the RB results is then decreased as the RB is evaluated far outside the domain of the snapshot data. Also, the enhanced robustness is still limited and an occasional lack of convergence for (large) magnitudes of certain kinds of deformations is to be expected.

Algorithm 4. Reduced Basis sub-routine **RB** $_N$

input Reduced Basis \mathcal{B} with $|N_{\text{RB}}|$; numbers of load directions $N_{\text{dir}}^{\text{eval}}$ and of load magnitudes $N_{\text{mag}}^{\text{eval}}$, scaling factor J^* of the Hencky strain basis; maximum load magnitude T_{max} ; load directions $\{\underline{N}^{(n)}\}_{n=1, \dots, N_{\text{dir}}^{\text{eval}}} \subset \mathbb{S}^6$; load magnitudes $\{t_m\}_{m=1, \dots, N_{\text{mag}}^{\text{eval}}} \subset [0, T_{\text{max}}]$; RVE Ω_0

initialize Concentric Interpolation support data $D = \{ \}$; extrapolation counter $N_{\text{ext}}^{\text{eval}} = 0$

for $n = 1, \dots, N_{\text{dir}}^{\text{eval}}$ **do** ▷ loop directions

for $m = 1, \dots, N_{\text{mag}}^{\text{eval}}$ **do** ▷ loop magnitudes

$\underline{U} = \exp\left(t_m \sum_{i=1}^6 N_i^{(n)} \underline{Y}^{(i)}\right)$ $\left(\underline{Y}^{(i)} \in \mathcal{Y}_{J^*}\right)$ ▷ boundary condition

 try to solve minimization task (25) with boundary condition \underline{U} using \mathcal{B}

if convergence **then**

 compute effective stress $\underline{S}_{\text{RB}}^{(N+1)}$ according to (27) and effective stiffness $\underline{C}_{\text{RB}}^{(N+1)}$ according to (28)

else

 linearly extrapolate $\underline{S}_{\text{RB}}^{(N+1)}$ and $\underline{C}_{\text{RB}}^{(N+1)}$ in t from magnitudes t_{m-2}, t_{m-1} (assume convergence at least for $m = 2$)

 increase extrapolation counter $N_{\text{ext}}^{\text{eval}} \leftarrow N_{\text{ext}}^{\text{eval}} + 1$

end if

 subtract initial stiffness (i.e., at $t = 0$) from current stiffness: $\underline{C}'_{\text{RB}} = \underline{C}_{\text{RB}}^{(N+1)} - \underline{C}_{\text{RB}}^{\text{ini}}$

 include vectorized support data in list, $D \leftarrow D \cup \left\{ \left(\underline{S}_{\text{RB}}^{(N+1)}; \underline{C}'_{\text{RB}} \right) \in \mathbb{R}^{6+21} \right\}$

end for

end for

output Concentric Interpolation support data D

Convergence in this context is defined as the RB residual (see Equation (28) of Reference 12) reaching a norm of less than $5 \cdot 10^{-7} \text{MPa} \cdot L^2$ (where L is the side length of the cubic RVE). Alternatively, convergence is assumed when the ratio of the residual to the current increment's initial residual is below 10^{-7} .

In contrast to the **FE** $_N$, where partly unsuccessfully applied BCs simply reduced the number of snapshots, this is a more severe issue for the **RB** $_N$: the outputs of this stage serve as inputs to the subsequent CI scheme. The latter necessarily requires data at all support points (with the current assumption of piecewise linear interpolants with identical support positions along all directions). We choose to linearly extrapolate incomplete RB data along the respective direction. The number of such interpolated RB results is counted in $N_{\text{ext}}^{\text{eval}}$. Alternatively, any other means of data completion could be employed, for example, by means of specific choices of the radial data functions $p_i(t)$ from Equation (32).

Note that just like the FE method, the RB method is suitable for trivial parallelization by simply running multiple instances of the program at the same time, each with different sets of BCs.

3.5.4 | User-defined material function based on Concentric Interpolation

As the last step before the completion of one homogenization loop in Figure 1, the \mathbf{CI}_N scheme is set up according to Equation (35). The interpolant \tilde{f} is incorporated in the user-defined material (Algorithm 5). Finally, the scale counter N is incremented by one and Algorithm 1 proceeds correspondingly.

Algorithm 5. User-defined material function of $\mathbf{FE}_{(N+1)}$ and of $\mathbf{RB}_{(N+1)}$, wrapping \mathbf{CI}_N

input right Cauchy-Green tensor $\mathbf{C}^{(N+1)}$; initial stiffness $\mathbf{C}_{\text{RB}}^{\text{ini}(N+1)}$ (constant); scale factor J^* of the basis $\mathcal{Y}(J^*)$ (constant)	
compute $\mathbf{E}^{(N+1)} = \frac{1}{2} \log \left(\mathbf{C}^{(N+1)} \right)$	▷ Hencky strain
transform $\mathbf{E}^{(N+1)}$ by (4) and (5) $\rightarrow \underline{N}, t$	▷ direction and magnitude w.r.t. basis $\mathcal{Y}(J^*)$
evaluate the \mathbf{CI}_N interpolant \tilde{f} at $(\underline{N}, t) \rightarrow \underline{S}_{\text{CI}}^{(N+1)}, \underline{C}'_{\text{CI}}^{(N+1)}$	▷ stress and shifted stiffness (cf. Algorithm~4)
output stress $\underline{S}_{\text{CI}}^{(N+1)}$ and stiffness $\underline{C}_{\text{CI}}^{(N+1)} = \underline{C}'_{\text{CI}}^{(N+1)} + \underline{C}_{\text{RB}}^{\text{ini}(N+1)}$	▷ stress and correct stiffness

4 | NUMERICAL EXAMPLES

4.1 | Three-scale homogenization of fractal structures on standard workstations

4.1.1 | Goals

The main goal of the following considerations is to provide an example of a three-scale simulation based on Algorithm 1, cf. Figure 1. This is meant as a proof of concept only and thorough investigations of important details, such as the influences of different kinds of parameters, are not within the current scope. The geometries of the RVEs on Scales 0 and 1 are identical. On Scale 2, the same geometry is again utilized. In this sense, the geometric setup (cf. Table 1, *top*) is of self-similar fractal kind. Roughly comparable scenarios were recently considered in other works.³⁴

If the geometry on Scale 2 is again considered an RVE and no body forces are applied, the resulting local stress field may be volume averaged and then interpreted as a fourth-scale homogenized quantity. This subsection ends with selected evaluations of such stresses on a hypothetical Scale 3.

4.1.2 | Geometry and Scale 0 model

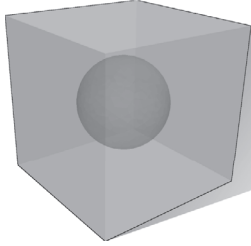
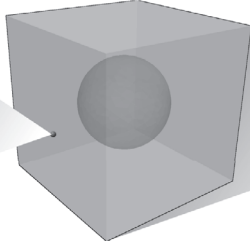
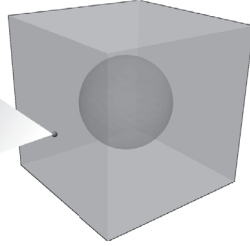
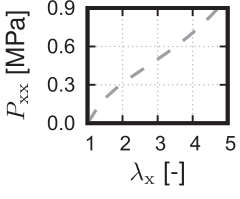
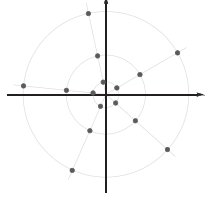
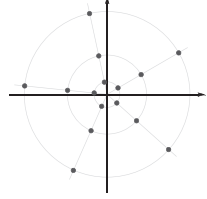
The geometry considered on all three scales is a cube with a centered spherical void, cf. Figure 3. The mesh contains 4399 second-order TET10 elements with a total of 7531 nodes resulting in almost 22 600 DOF. The mesh, that is, the solid phase, occupies a volume of 0.90 within the unit cube.

For the material law on Scale 0, the extended tube model (ETM) (eq. (22) of Reference 35) together with a mixed quadratic-logarithmic volumetric model³⁶ is utilized:

$$W_C(\mathbf{C}) = W_{\text{ETM}}(J^{-2/3}\mathbf{C}) + \frac{K}{4}((J-1)^2 + \log(J)^2). \quad (37)$$

As found by a comparative study (table III of Reference 37), the ETM is a realistic model of rubber-like materials for the parameters $G_c = 0.202$ MPa, $G_e = 0.153$ MPa, $\beta = 0.178$ MPa, $\delta = 0.0856$ MPa, which are therefore employed in the present work. The bulk modulus-like parameter K is empirically chosen as $K = 10$ MPa in order to set a high ratio to the

TABLE 1 Three-scale setup: geometry and parameters [Colour figure can be viewed at wileyonlinelibrary.com]

	 Scale 0	 Scale 1	 Scale 2
field variables	E, S, C, \dots	$\bar{E}, \bar{S}, \bar{C}, \dots$	$\bar{\bar{E}}, \bar{\bar{S}}, \bar{\bar{C}}, \dots$
boundary condition	$\bar{U} = \exp(\bar{E})$	$\bar{\bar{U}} = \exp(\bar{\bar{E}})$	$\bar{\bar{\bar{U}}} = \exp(\bar{\bar{\bar{E}}})$ or arbitrary
material law	ETM 	CI_0 	CI_1 
FE parameters	FE_0: $N_{dir}^{eval} = 100$ $N_{mag}^{eval} = 10$ $J^* = 1.2$ $T_{max} = 1.0$	FE_1: $N_{dir}^{eval} = 100$ $N_{mag}^{eval} = 10$ $J^* = 1.2$ $T_{max} = 0.3$	
POD parameters	POD_0: $N_{snap} = 956$ $N_{RB} = 30$	POD_1: $N_{snap} = 957$ $N_{RB} = 30$	
RB parameters	RB_0: $N_{dir}^{eval} = 500$ $N_{mag}^{eval} = 20$ $J^* = 1.2$ $T_{max} = 1.0$	RB_1: $N_{dir}^{eval} = 500$ $N_{mag}^{eval} = 20$ $J^* = 1.2$ $T_{max} = 1.0$	
RB results extrapolation	$N_{ext}^{eval} = 94$	$N_{ext}^{eval} = 1438$	
CI parameters	CI_0: $N_{dir}^{supp} = 500$ $N_{mag}^{supp} = 20$	CI_1: $N_{dir}^{supp} = 500$ $N_{mag}^{supp} = 20$	
CI action	$\frac{\gamma}{E} \mapsto \bar{S}_{CI}, \bar{C}_{CI}$	$\frac{\gamma}{E} \mapsto \bar{\bar{S}}_{CI}, \bar{\bar{C}}_{CI}$	

other parameters and, thereby, to approach quasi-incompressible behavior. A nonlinearity that is more pronounced with the ETM than with the widely used Neo-Hookean model is visible in Figure 4.

4.1.3 | Three-scale setup

According to Algorithm 1 and Figure 1, the homogenization of Scale 0 and of Scale 1 is performed in a staged manner. All parameters employed throughout this homogenization process are listed in Table 1.

FIGURE 3 Geometry of the cubic structure with a centered spherical void. The volume fraction of the void is 10% [Colour figure can be viewed at wileyonlinelibrary.com]

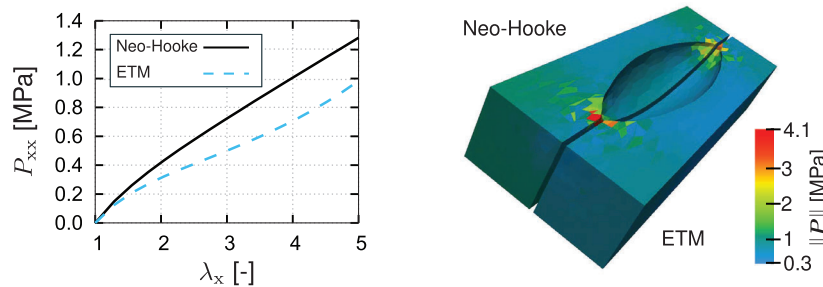
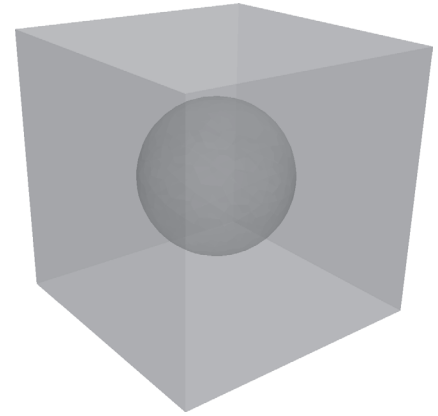


FIGURE 4 Comparison of the Neo-Hookean and the Extended Tube Model under isochoric uniaxial extension. As for the ETM, the Neo-Hookean material parameter is chosen from a comparative study (table III of Reference 37). *Left*: evolution of the principal stress over the principal stretch. *Right*: composite image consisting of two cut-out quarters of the deformed voided microstructure for comparison of the influences of the different material laws. Coloring indicates the magnitude of the first Piola-Kirchhoff stress per integration point

The kernel width parameter γ is determined via optimization of the stresses $\bar{\mathbf{S}}_{\text{CI}}$ with respect to validation stresses $\bar{\mathbf{S}}_{\text{RB}}$ on a large set of validation Hencky strains: $N_{\text{dir}}^{\text{eval}} = 1000$, $N_{\text{mag}}^{\text{eval}} = 100$, $J^* = 1.2$, $T_{\text{max}} = 1.0$. For comparison, the optimization of the kernel parameter γ yields an optimal value of $\gamma = 3.56$ when the discrepancy between the stiffnesses $\bar{\mathbb{C}}_{\text{CI}}$ and $\bar{\mathbb{C}}_{\text{RB}}$ is minimized. As the stress approximation directly influences the balance equation, the result obtained from the stress optimization is employed. The same value of γ is used for the interpolation scheme **CI_1** without further optimization.

Another noteworthy parameter is T_{max} , which is 1.0 throughout Scale 0. However, it is reduced for **FE_1** to $T_{\text{max}} = 0.3$ due to severe convergence issues, cf. Section 3.5.1. The enhanced robustness of **RB_1**, cf. 3.5.3, allows for the choice of $T_{\text{max}} = 1.0$ again. At this stage, $14\% \approx N_{\text{ext}}^{\text{eval}} / (N_{\text{dir}}^{\text{eval}} N_{\text{mag}}^{\text{eval}})$ of the applied BC lacked RB convergence.

4.1.4 | Hardware setup and runtimes

In order to accelerate the setup phase (or offline phase), the FE, POD, and RB computations were performed on a standard workstation with an Intel (R) Xeon (R) E5-2643 v3 CPU (12 threads) and 256 Gb of RAM. The memory intensive POD never came close to requiring all memory.

An exact quantitative comparison of the various runtimes is not within the scope of the current work. Depending on the method and on the stage, different kinds of overhead data were created and stored during the multi-scale homogenization process, for example, visualization data, statistics, and debugging information. Also, important meta-parameters were chosen as sophisticated guesses, for example, stopping criteria, maximum number of Newton iterations, behavior in case of convergence failure. Furthermore, the FE and the RB simulations were conducted with multiple instances of the same program running in parallel, each with a different set of BCs. Most importantly, the computations for the current case study were not always conducted on a dedicated workstation. For these reasons, quantitatively exactly reproducible runtime values are set aside for the moment. The overall wall time to conduct the whole three-scale homogenization

procedure on the workstation, that is, for **FE_0**, **POD_0**, **RB_0**, **FE_1**, **POD_1**, and **RB_1** together, was approximately 7 hours. The simulations on the third scale by means of **FE_2** were conducted on a laptop computer and took approximately 2-3 minutes per load path.

4.1.5 | Results

As the overall porosity of the structure increases with each homogenized scale, a *scale softening effect* is observed in the initial stiffnesses, that is, in the stiffness tensors at zero magnitude, $t = 0$, cf. Table 2.

Next, the geometrically identical structures on Scales 0, 1, and 2 are subjected to the same BC, $\bar{\mathbf{U}} = \bar{\bar{\mathbf{U}}} = \bar{\bar{\bar{\mathbf{U}}}}$, with the principal stretches $\lambda_x = \lambda_z = 0.9035$, $\lambda_y = 1.225$. The resulting deformations and stress distributions are depicted in Figure 5. The effect of the scale softening is clearly visible which is in accordance with Table 2.

We now address the question of *how reduced bases of two scales compare to each other*. Although they are returned from identical routines **POD_0** and **POD_1**, their underlying snapshot data differs in terms of the material law and, most significantly, the parameter T_{\max} . Since the eigenvectors of the snapshot correlation matrix are ordered descendingly with respect to the corresponding eigenvalues, the returned $N_{\text{RB}} = 30$ RB elements represent the most significant information contained in the snapshots. Out of this set, the first nine functions are depicted in Figure 6 for both scales.

A systematic comparison of the two bases is possible when considering the *absolute correlation of the reduced bases*, that is, the mutual projections of the RB elements onto each other, $|\langle \mathbf{B}^{(i)} \cdot \bar{\mathbf{B}}^{(j)} \rangle|$. This is well-defined, cf. Equation (10), when considering that the geometries of the RVE are identical, $\bar{\bar{\Omega}}_0 = \bar{\bar{\bar{\Omega}}}_0$. The RB correlations are visualized in Figure 7

These correlation values reveal some similarities that one might expect from visual inspection of Figure 6, for example, $\mathbf{B}^{(4)} \leftrightarrow \bar{\mathbf{B}}^{(6)}$ and $\mathbf{B}^{(6)} \leftrightarrow \bar{\mathbf{B}}^{(5)}$. Moreover, some less obvious relationship are found, for example, $\mathbf{B}^{(5)} \leftrightarrow \bar{\mathbf{B}}^{(4)}$. One should bear in mind that the visualization in Figure 6 might appear differently if another clipping plane was chosen.

Next, the **accuracy** of **RB_N** and **CI_N** is compared against **FE_N** for $N = 0$ and $N = 1$. Recall the definition of the homogenized stress from Equation(20). For $N = 0$, a set of CS BCs $\bar{\mathcal{E}}_{\text{vali}}$ are chosen with the parameters $T_{\max} = 0.3$, $J^* = 1.2$, $N_{\text{dir}}^{\text{eval}} = 150$, and $N_{\text{mag}}^{\text{eval}} = 10$, that is, $|\bar{\mathcal{E}}| = 1500$. The same CS parameters are chosen for $\bar{\bar{\mathcal{E}}}_{\text{vali}}$ and $N = 1$. However, this set is reduced to contain only those BCs for which **FE_1** successfully converges, wherefore effectively $|\bar{\bar{\mathcal{E}}}_{\text{vali}}| = 1437$.

TABLE 2 Initial stiffness matrices (ie, for $t=0$) of the ETM and as output of **RB_0** and **RB_1**

$\bar{\bar{\mathbf{C}}}_{\text{ETM}}^{\text{ini}}$ [MPa] =	$\bar{\bar{\mathbf{C}}}_{\text{RB}}^{\text{ini}}$ [MPa] =	$\bar{\bar{\bar{\mathbf{C}}}}_{\text{RB}}^{\text{ini}}$ [MPa] =
$\begin{bmatrix} 10.59.77 & 9.770 & 00 \\ 10.5 & 9.770 & 00 \\ & 10.50 & 00 \\ & & 0.704 & 00 \\ \text{sym} & & & 0.7040 \\ & & & & 0.704 \end{bmatrix}$	$\begin{bmatrix} 3.77 & 3.09 & 3.09 & 1.22 \cdot 10^{-3} & 7.74 \cdot 10^{-4} & 3.74 \cdot 10^{-4} \\ & 3.77 & 3.09 & 8.58 \cdot 10^{-4} & 1.10 \cdot 10^{-3} & 1.18 \cdot 10^{-3} \\ & & 3.77 & 6.38 \cdot 10^{-4} & 9.37 \cdot 10^{-4} & 8.44 \cdot 10^{-4} \\ & & & 0.654 & -4.02 \cdot 10^{-5} & 2.15 \cdot 10^{-4} \\ \text{sym} & & & & 0.653 & 3.21 \cdot 10^{-4} \\ & & & & & & 0.653 \end{bmatrix}$	$\begin{bmatrix} 2.34 & 1.69 & 1.69 & 8.89 \cdot 10^{-4} & 5.94 \cdot 10^{-4} & 5.48 \cdot 10^{-5} \\ & 2.34 & 1.69 & 5.85 \cdot 10^{-4} & 8.68 \cdot 10^{-4} & 7.74 \cdot 10^{-4} \\ & & 2.34 & 3.97 \cdot 10^{-4} & 7.43 \cdot 10^{-4} & 4.68 \cdot 10^{-4} \\ & & & 0.602 & -5.57 \cdot 10^{-5} & 9.85 \cdot 10^{-5} \\ \text{sym} & & & & 0.600 & 2.62 \cdot 10^{-4} \\ & & & & & & 0.601 \end{bmatrix}$

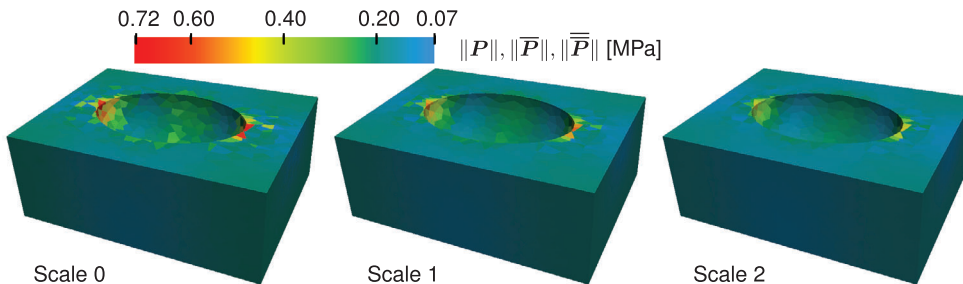


FIGURE 5 Half sections of the porous structures on three scales, subject to isochoric uniaxial extension with the principal stretches $\lambda_x = \lambda_z = 0.9035$, $\lambda_y = 1.225$. Coloring indicates the stress magnitude per integration point

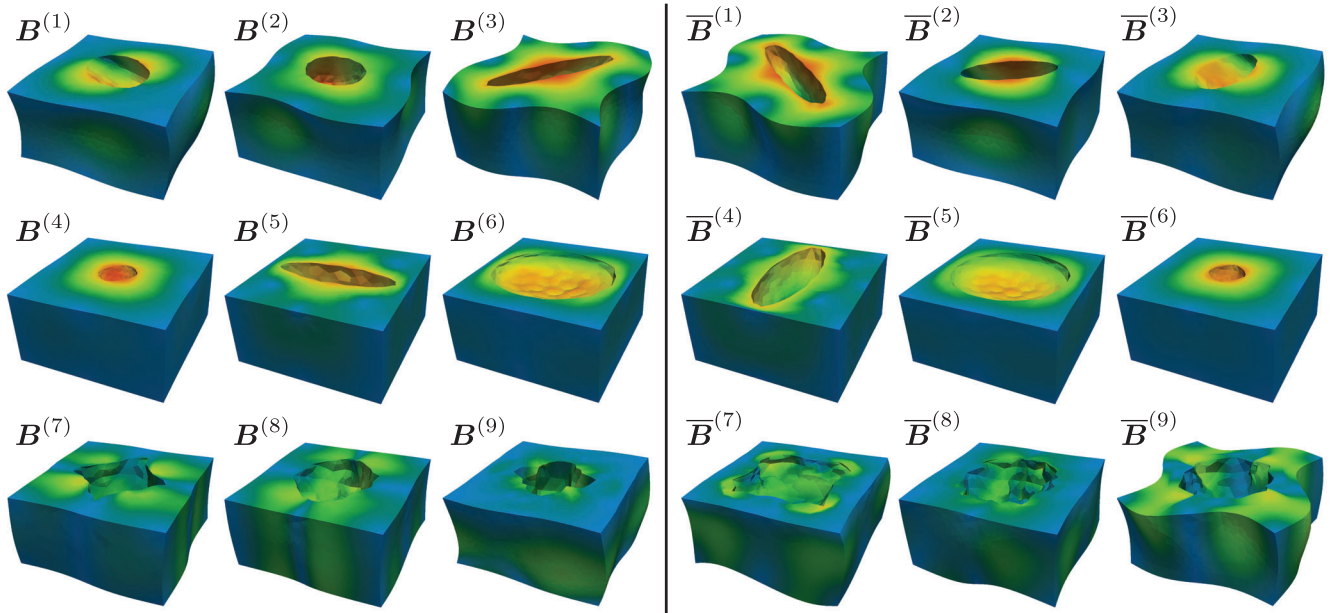
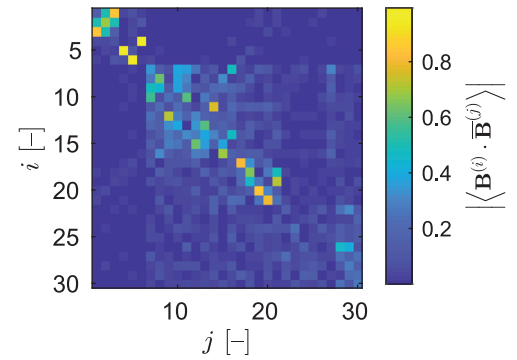


FIGURE 6 Lower halves of the deformation patterns corresponding to the first nine of the 30 Reduced Basis functions on Scale 0 (*left*) and on Scale 1 (*right*). Coloring indicates displacement magnitude. See also Figure 7

FIGURE 7 Correlations of the Reduced Bases $\mathbf{B}^{(1)}, \dots, \mathbf{B}^{(30)}$ and $\bar{\mathbf{B}}^{(1)}, \dots, \bar{\mathbf{B}}^{(30)}$ of Scales 0 and 1, respectively. See also Figure 6



The set of relative errors

$$\text{err} \left(\mathbf{P}_{\bullet}, \mathbf{P}_{\text{FE}}, \mathcal{E}_{\text{vali}} \right) = \left\{ \frac{\| \mathbf{P}_{\bullet}(\mathbf{E}) - \mathbf{P}_{\text{FE}}(\mathbf{E}) \|}{\| \mathbf{P}_{\text{FE}}(\mathbf{E}) \|} \mid \mathbf{E} \in \mathcal{E}_{\text{vali}} \right\} \quad (N = 1, 2; \bullet = \text{RB, CI}), \quad (38)$$

is considered. The corresponding empirical distribution functions are shown in Figure 8. One should keep in mind that **FE_1** (and **RB_1**) utilizes **CI_0** as a material law. Hence, the comparison in Figure 8 (*right*) is with respect to an approximate reference.

In any case, it is observed that the error in the stress approximation is within acceptable bounds ($\leq 8\%$ on Scale 1, $\leq 1\%$ on Scale 2). This has to be seen in the context of actual engineering applications where many other additional uncertainties come into play, such as the material models on Scale 0 and the geometry of the considered RVEs.

Eventually, a couple of *four-scale simulations* are conducted. Isochoric uniaxial extension BCs of the kind

$$\bar{\mathbf{U}} = \bar{\underline{\underline{\mathbf{U}}}} = \bar{\underline{\underline{\mathbf{U}}}} = \exp(t \mathbf{Y}^{(1)}) \quad (\mathbf{Y}^{(1)} \leftrightarrow \underline{\underline{\mathbf{Y}}}, \text{cf. (2)}), \quad (39)$$

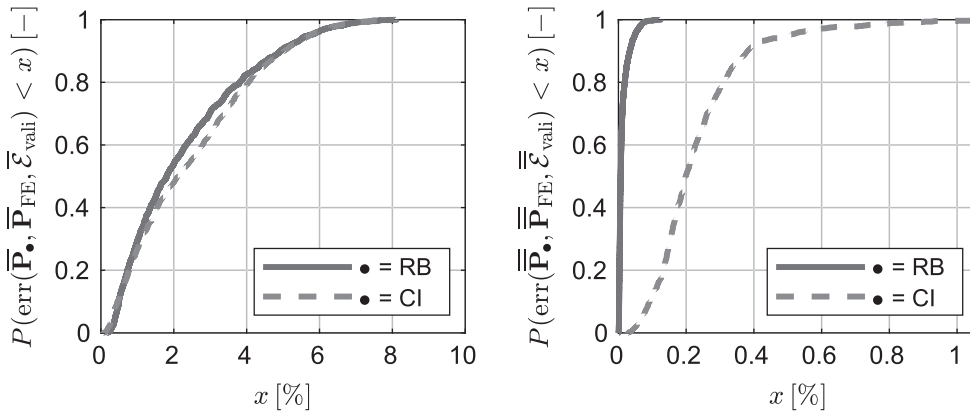


FIGURE 8 Empirical distribution functions of the relative error of the first Piola-Kirchhoff stress on Scale 1 (left) and on Scale 2 (right) as homogenized results of the FE_N , RB_N , and CI_N methods with $N = 0, 1$, respectively [Colour figure can be viewed at wileyonlinelibrary.com]

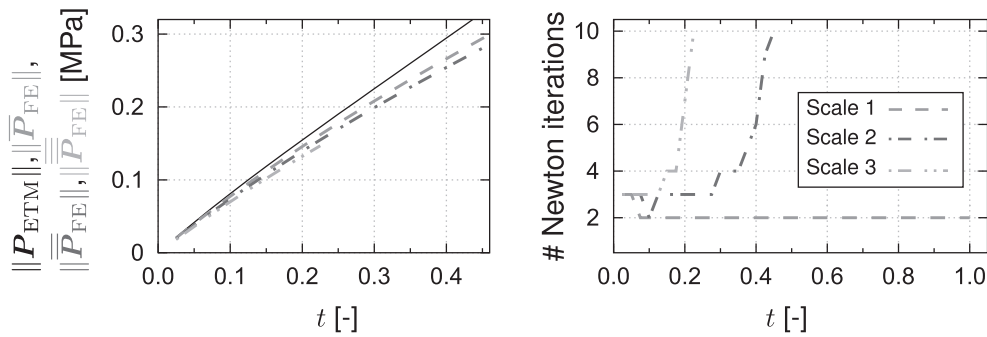


FIGURE 9 Evolution of stress magnitudes on Scales 0-3 (left) and of the number of Newton iterations of the corresponding FEM (right) over the magnitude t of the uniaxial isochoric extension boundary condition [Colour figure can be viewed at wileyonlinelibrary.com]

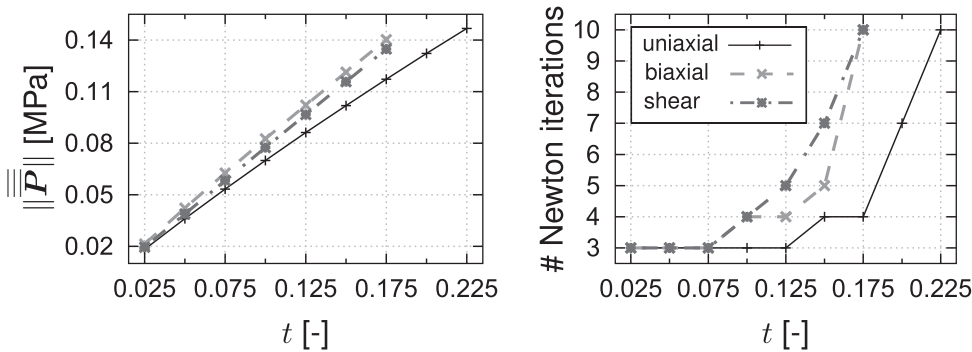


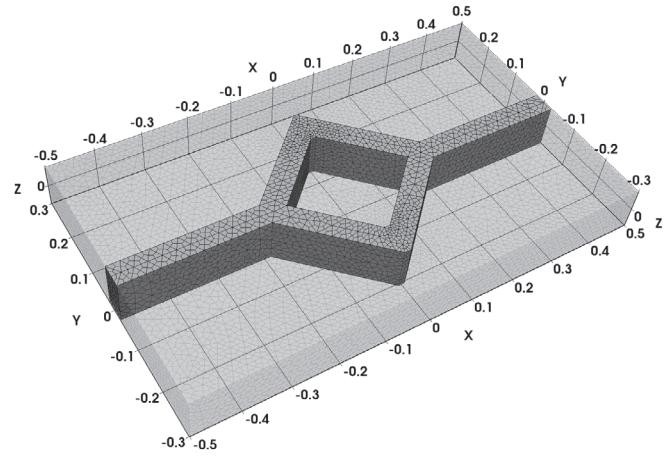
FIGURE 10 Evolution of the effective stress (left) and of the number of Newton iterations of the FEM (right) on Scale 3 over the boundary condition magnitude [Colour figure can be viewed at wileyonlinelibrary.com]

with $t \in [0, 1]$, are applied to the three Scales 0, 1, and 2. The respective FE methods are invoked and the resulting stress fields $\mathbf{P}(\mathbf{X})$, $\bar{\mathbf{P}}(\bar{\mathbf{X}})$, and $\bar{\bar{\mathbf{P}}}(\bar{\bar{\mathbf{X}}})$, respectively, are computed. Subsequently, these are volume averaged, leading to $\bar{\mathbf{P}}$, $\bar{\bar{\mathbf{P}}}$, and $\bar{\bar{\bar{\mathbf{P}}}}$ which are quantities on Scales 1, 2, and 3, respectively (counted to base zero). The magnitudes of these effective stresses are depicted in Figure 9 (left). The amount of corresponding Newton iterations is graphed in Figure 9 (right).

By the number of iterations and by the maximum value of the magnitude t for which FE convergence is obtained, one can clearly see a trend of deteriorating FE convergence as more scales are homogenized, cf. Section 3.5.1. Also, the scale softening effect is again noticeable.

More kinds of fourth scale BCs $\bar{\bar{\bar{\mathbf{U}}}} = \exp(t \mathbf{Y}^{(i)})$ are applied to Scale 2. The evolution of the volume-averaged stresses for the choices $i = 1, 2, 3$ is shown in Figure 10 (left), with the corresponding Newton iteration count on the right.

FIGURE 11 Geometry and graded FE mesh of periodic microstructure with hash-shaped inclusion [Colour figure can be viewed at wileyonlinelibrary.com]



As the maximum magnitude is comparatively low, $t = 0.175$, respectively, $t = 0.225$, the resulting stress curves appear almost linear. Nonetheless, the capability of the proposed scheme to perform *four-scale simulations on laptop computers* is successfully demonstrated.

4.2 | Homogenized stress response of stiffening microstructure via CI

4.2.1 | Goals

The aims of this numerical example are to

- prove the suitability of the CI method for the homogenization of a highly anisotropic RVE, that is, homogenize one scale only,
- modify the CI interpolant $\tilde{f} : \mathbb{R}^6 \rightarrow \mathbb{R}^9$ such that it interpolates the stress $\bar{\mathbf{P}}$ as a function of the Hencky strain $\bar{\mathbf{E}}$,
- setup the CI interpolant directly on FE data, avoiding the offline stages POD and RB as far as possible,
- gain insights into the influence of the parameters $N_{\text{dir}}^{\text{supp}}$ and γ on the accuracy of the stress interpolation,
- study the influence of the parameter $N_{\text{dir}}^{\text{supp}}$ on the runtime of the CI scheme.

This subsection does *not* strictly employ Algorithm 1 but instead investigates the possible shortcut FE \rightarrow CI. As pointed out in Section 2.2.2, the FE method is not nearly as well suited as the RB for providing the tangent modulus, hence we now focus on the stress only.

4.2.2 | Model

The RVE under consideration is depicted in Figure 11. The FE mesh of the noncubic RVE consists of quadratic TET10 elements with a total of 33 923 nodes, resulting in over 10^5 total DOF. The hash-shaped inclusion phase has a volume fraction of 13.3% and is the source of significant geometric stiffening effects under certain BCs, as was investigated previously.¹²

An isochoric Neo-Hookean material law together with a mixed logarithmic-quadratic volumetric part³⁶ of the form

$$W_{\mathbf{C}}(\mathbf{C}) = \frac{G}{2}(\text{trace}(J^{-2/3}\mathbf{C}) - 3) + \frac{K}{4}((J - 1)^2 + \log((J)^2)), \quad (40)$$

is employed for both the inclusion and the surrounding matrix phase. While $G_{\text{m}} = 10$ MPa and $K_{\text{m}} = 3000$ MPa are chosen for the latter, the former is described by the constants $G_{\text{i}} = 100$ MPa and $K_{\text{m}} = 3000$ MPa, that is, the phase contrast is 10 for the shear modulus. These material parameters roughly correspond to a soft polymer matrix and a stiffer polymer inclusion.

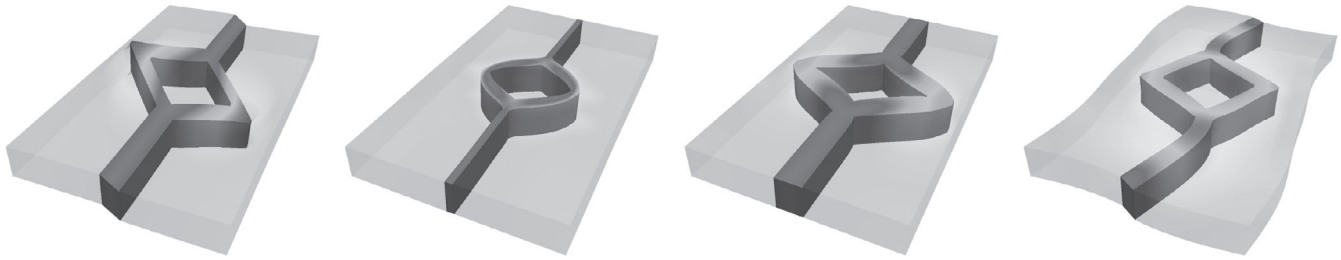


FIGURE 12 Displacement fields corresponding to some Reduced Basis elements. Coloring indicates displacement magnitude [Colour figure can be viewed at wileyonlinelibrary.com]

As before, it is important to emphasize that the choice of the hyperelastic material model is completely arbitrary and serves as an example only. The method is general with respect to this choice.

4.2.3 | Design of the interpolation scheme

For this example, the domain of interest within the Hencky space is defined via $T_{\max} = 1$ and $J^* = 1.005$. Initially, it is assumed that a sufficiently accurate interpolant $\bar{\mathbf{P}}_{\text{CI}}$ of the effective stress $\bar{\mathbf{P}}$ should be attainable with $N_{\text{dir}}^{\text{supp}}$ between 50 and 1000. The supporting magnitudes are chosen at $N_{\text{mag}}^{\text{supp}} = 10$ values, wherefore the total numbers of supporting points lie between 500 and 10 000. If instead, for example, regular Cartesian grids were employed, the same total numbers of points p^6 would imply as few as $p \approx 2.8$ to $p \approx 4.7$ points along each axis.

The $N_{\text{mag}}^{\text{supp}} = 10$ supporting magnitudes are chosen as 0.1, ..., 0.9, 1.0. The number of supporting directions $N_{\text{dir}}^{\text{supp}}$ takes the values 50, 100, 200, 250, 500, 1000. These sets of directions are mutually independent, that is, no intersections and especially no hierarchies are enforced.

In this example, a direct setup of the CI scheme is pursued, that is, based on FE data in order to circumvent the offline stages POD and RB. However, due to the complexity of the microstructure, only the supporting points of the CI schemes with $N_{\text{dir}}^{\text{supp}} = 50, 100, 200$ are computed by means of the FEM.

For the larger values of $N_{\text{dir}}^{\text{supp}}$, the original Algorithm 1 is made use of. For the corresponding POD, the support data of the CI scheme with $N_{\text{dir}}^{\text{supp}} = 200$ is taken as snapshot data \mathcal{S} . The results are again truncated at $N_{\text{RB}} = 30$, which is based on experience with an RVE of the same geometry.¹² Some of the RB elements are visualized in Figure 12. This RB model is employed for the creation of the supporting data of the CI schemes with $N_{\text{dir}}^{\text{supp}} = 250, 500, 1000$.

4.2.4 | Evaluation and results

A validation set of response stresses $\bar{\mathbf{P}}_{\text{FE}}$ is created at additional Hencky strain sampling sites (i.e., disjoint from the training sites) parametrized by $N_{\text{dir}}^{\text{eval}} = 150$ and $N_{\text{mag}}^{\text{eval}} = 16$, where the magnitudes are of the form $t^{(i)} = i/16, i = 1, \dots, N_{\text{mag}}^{\text{eval}}$. Of these $150 \cdot 16 = 2400$ evaluation points, 17 are excluded due to a lack of convergence of the FEM, cf. Section 3.5.1. Therefore, here, the validation set $\bar{\mathcal{E}}_{\text{vali}}$ consists of 2383 FE-homogenized stresses corresponding to an incomplete set of concentric samples of Hencky strains $\bar{\mathbf{E}}$.

In order to assess the accuracy of the interpolant $\bar{\mathbf{P}}_{\text{CI}}$ compared to the result $\bar{\mathbf{P}}$ of the FEM, the error measure

$$\text{err}_p = \frac{\|\bar{\mathbf{P}}_{\text{CI}} - \bar{\mathbf{P}}_{\text{FE}}\|}{\|\bar{\mathbf{P}}_{\text{FE}}\|}, \quad (41)$$

is evaluated on $\bar{\mathcal{E}}_{\text{vali}}$. With this at hand, the quality of a given kernel parameter γ can be judged. Figure 13 visualizes the influence of this parameter on the overall error for each of the chosen number of supporting directions.

One can observe an increase of the minimum mean error from $N_{\text{dir}}^{\text{supp}} = 200$ to $N_{\text{dir}}^{\text{supp}} = 250$. This observation is interpreted as the effect of the additional error introduced by the RB approximation in the latter case.

FIGURE 13 Mean value of the stress error function of Equation (41) on the set of 2383 validation points

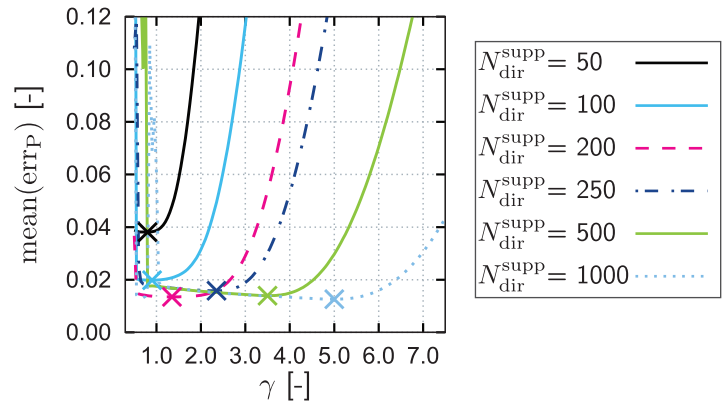
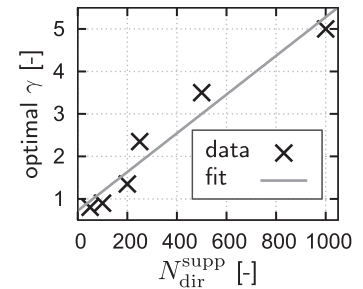


FIGURE 14 Values of the kernel parameter γ as results from the conducted optimizations (points, cf. Figure 13) and the result of a linear least squares regression (line, cf. Equation (42)) [Colour figure can be viewed at wileyonlinelibrary.com]



As is well-known (sec. 7 of Reference 21), very small values of γ render the method numerically unstable and lead to volatile results. For small numbers of supporting directions, the optimum value marks the beginning of the numerically stable domain, for example, as is the case for $N_{\text{dir}}^{\text{supp}} = 50$. As the number of supporting directions increases, the best value of γ increases, shifting into the interior of the numerically stable domain, for example, as is the case for $N_{\text{dir}}^{\text{supp}} = 1000$.

An important property of the CI method is that changes to the minimum mean error value with respect to the kernel parameter are marginal within a notably large neighborhood of the optimum. This confirms an empirical finding of the original study of the small strain equivalent method (p. 212 of Reference 22): the kernel parameter may be fixed at $\gamma = 2.0$ for a wide range of $N_{\text{dir}}^{\text{supp}}$ without pronounced loss of accuracy. The found optimum values of the present examples are visualized in Figure 14. A linear least squares regression of these data points yields the approximate relationship

$$\gamma(N_{\text{dir}}^{\text{supp}}) \approx 0.00456 N_{\text{dir}}^{\text{supp}} + 0.7208. \quad (42)$$

Next, the distribution of the function err_P is studied for these optimum γ values. To this end, Figure 15 shows the empirical distribution functions (EDFs) of this error quantity for each value of $N_{\text{dir}}^{\text{supp}}$ and for each evaluation magnitude. In other words, the EDFs measure the probability, for each evaluation magnitude separately, of the error lying within certain bounds when evaluated at any of the $N_{\text{dir}}^{\text{eval}} = 150$ directions.

One can observe that the mean of the error err_P is below 2% for as few as $N_{\text{dir}}^{\text{supp}} = 100$ supporting directions. Also, the individual EDFs are comparatively “smooth,” that is, they do not exhibit significant jumps or plateaus. This confirms a lack of severe outliers of the error function (41).

It is worth noticing that, just as with the results depicted in Figure 13, the mean of the error seems to be decreasing monotonically with an increasing number of supporting directions, except for the transition from $N_{\text{dir}}^{\text{supp}} = 200$ to $N_{\text{dir}}^{\text{supp}} = 250$. This is very likely due to the additional error introduced by the RB, slightly deteriorating the quality of the data at the supporting points. Still, a further increasing number of supporting directions leads, again, to a monotonic decrease of the mean error. In terms of the mean error, parity of the RB-based CI scheme with the finest FE-based CI scheme is only reached with $N_{\text{dir}} > 500$. However, even with $N_{\text{dir}}^{\text{supp}} = 1000$ the ROM-based CI scheme is notably more prone to the maximum error than the FEM-based one with just one-fifth as many supporting points.

Finally, the average CPU time of all CI evaluations on the validation set $\bar{\mathcal{E}}_{\text{vali}}$ are depicted in Figure 16 as a function of $N_{\text{dir}}^{\text{supp}}$. The average is taken with respect to 452 770 evaluations of the stress interpolant \bar{P}_{CI} (2383 evaluation Hencky

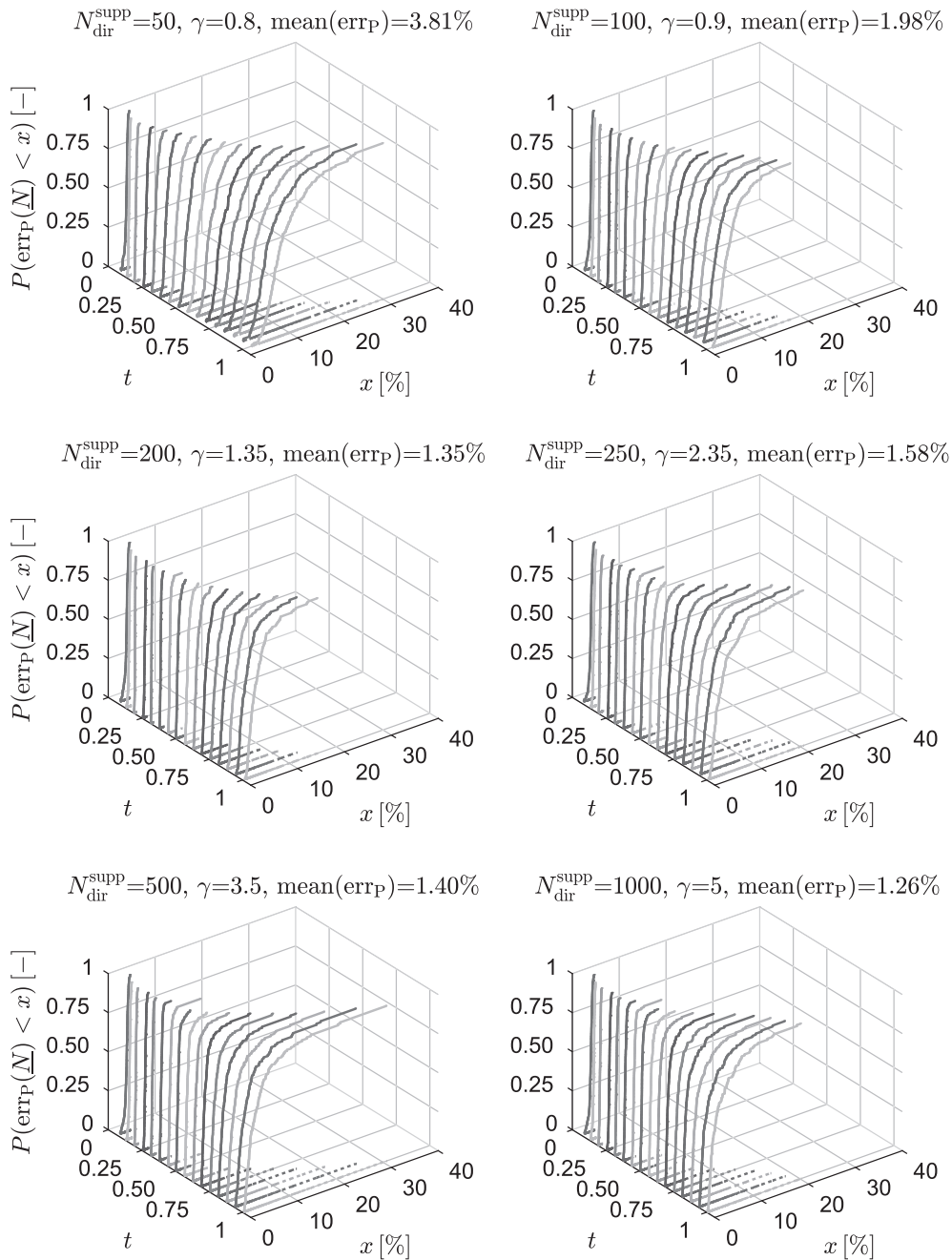


FIGURE 15 EDFs of stress error err_P of hash microstructure [Colour figure can be viewed at wileyonlinelibrary.com]

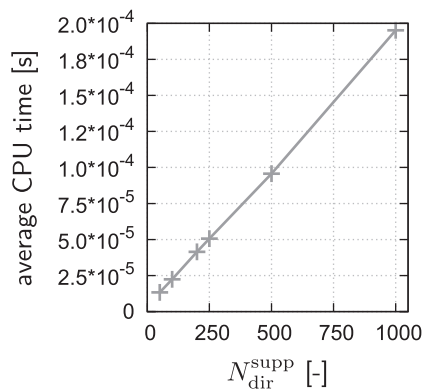


FIGURE 16 Average CPU time of a single evaluation of the stress interpolant \bar{P}_{CI} , as a function of the number of supporting directions $N_{\text{dir}}^{\text{supp}}$. The average is taken with respect to 452 770 evaluations [Colour figure can be viewed at wileyonlinelibrary.com]

strains and 190 different values of γ , cf. Figure 13). For these computations, a standard laptop computer was used. No parallelization was employed.

An almost linear relationship between the average CPU time T and $N_{\text{dir}}^{\text{supp}}$ can be observed, $T \approx 1.91 \cdot 10^{-7} \text{s} \cdot N_{\text{dir}}^{\text{supp}} + 2.91 \cdot 10^{-6} \text{s}$. The actual relation barely notably tends to superlinearity. These CPU times correspond to more than 5100 evaluations per second for $N_{\text{dir}}^{\text{supp}} = 1000$ and 75 000 evaluations per second for $N_{\text{dir}}^{\text{supp}} = 50$. In particular, CI enables 1 million evaluations of the homogenized finite strain constitutive model in only ~ 200 seconds ($N_{\text{dir}}^{\text{supp}} = 1000$) and in 14 seconds ($N_{\text{dir}}^{\text{supp}} = 50$), respectively.

5 | SUMMARY AND DISCUSSION

5.1 | Summary

A novel method for the homogenization of many spatial scales in finite strain hyperelasticity was successfully demonstrated. The combination of moderate, simple parallelization on standard workstations and efficient numerical methods rendered the offline homogenization across three scales possible within a couple of hours. The online phase was conducted on a laptop computer within a few minutes of compute time. Many thousands of evaluations of the numerical surrogate for the upscaled material response are evaluated per second.

Qualitatively, the observed results matched the expectations, that is, nested scales with porous RVEs resulted in a significant scale-softening effect. Also, a highly anisotropic RVE was homogenized with good accuracy.

The main challenge was a deteriorating convergence behavior for the larger scales. This is a widely-known issue that, to the best knowledge of the authors, is present in most if not all computational multi-scale methods. Additionally, the interplay of the many parameters for the main algorithm does not contribute to user-friendliness.

The workflow can possibly be significantly simplified and accelerated if one settles with interpolation of data generated directly by the FEM. This is especially viable when effective stiffnesses are not sought-after. As far as usability is concerned, it must be emphasized that the scheme is non-intrusive in the sense that it can be utilized with any simulation software that provides an interface to user-defined material routines.

5.2 | Interpolation given different strain measures

Sticking to the Hencky strain space for the sampling comes with many advantages. Most importantly, the Hencky strain space is isomorphic to the full space \mathbb{R}^6 while the spaces of other deformation or strain measures are isomorphic to nonlinear manifolds embedded into \mathbb{R}^6 (e.g., for \mathbf{C} , \mathbf{U}) and \mathbb{R}^9 (e.g., for \mathbf{F}) due to constraints on the tensors such as positive definiteness or preserved orientations. More precisely, any point in \mathbb{R}^6 will yield an admissible Hencky strain while for other deformation measures (independent of the chosen basis) additional checks on the admissibility are required. Furthermore, the Hencky strain allows to explicitly control the sampling of the determinant of \mathbf{F} in a straight-forward manner, which is a tricky procedure for other strain measures. It should be noted that regardless of what input strain is delivered, as long as the sampling is effected with respect to strain states corresponding to the CS points in the Hencky strain space, CI can be performed after transforming the input to the Hencky domain. However, this does not imply that the program calling the CI-based scheme must work with the Hencky strain. Note also that the validity of the samples in more obvious deformation measures (such as the right Cauchy Green strain) yields points for which the requested samples cannot be obtained, as discussed in other works.³⁰ Therefore, the authors decided to use and also to promote the use of CS in the Hencky strain space and the related CI although this choice is not intrinsically unique and explicitly not a rigorous requirement of CI.

5.3 | Number of sampling directions

From the results of Section 4.2, it is concluded that the gains in accuracy by a larger number of supporting directions is partly offset by the additional modeling error of the RB scheme. Moreover, this error comes along with significant additional offline costs for the identification and evaluation of the RB. Future investigations of the shortcut of directly interpolating high-fidelity data—if available—might be fruitful. The trade-off with respect to the resolution of anisotropic

effects may be a delicate choice. Note that by anisotropy, not just explicitly given material laws are meant but also geometry-induced effects on higher scales.

5.4 | Number and position of sampling magnitudes

Choosing the distribution of the $N_{\text{mag}}^{\text{supp}}$ radial supporting points relies on empiricism at the current state of the art. Variations of the qualitative distribution as well as variations of the number $N_{\text{mag}}^{\text{supp}}$ were exemplarily treated previously.^{21,22} It was found that CI is rather insensitive to the distribution of the supporting points and that an increase of their amount correlates with the quality of the interpolation. However, neither the positioning of the points nor the determination of their quantity can be rigorously guided at the moment, for example, by means of an error estimation.

5.5 | Kernel parameter

Also, the findings of Section 4.2 suggest that the determination of the optimum value of the kernel parameter γ may be omitted if the value is chosen according to Equation (42). The error induced by this possibly sub-optimal γ value may be justifiable depending on the context. An optimization of the kernel parameter should generally be conducted on data that is primary to the balance equations, that is, on stresses and not on tangent moduli or on energy densities. However, fitting to modulus data yielded a comparable result in the present study.

5.6 | Accuracy

Errors propagate exponentially through scales. As far as errors stemming from the data-driven approach are concerned, these might be assessed by performing unreduced FE² simulations—for a single scale transition. Concerning three or more scales, such unmodified schemes are practically impossible with meaningful spatial resolution at each scale, as the computational effort also grows exponentially with the number of scales. Furthermore, convergence issues with classical methods remain a serious hurdle, as was also experienced in the present work. Thus, the application of the RB method reduces the computational effort to a manageable level not just because of the numerical economy but also due to the increased numerical robustness. Because of the latter, larger load increments are possible and, as we experienced, certain load levels become computationally feasible. For growing load magnitudes, the accuracy of the CI-model tends to decrease. This effect was investigated in previous works (fig. 12 of Reference 21). There, it was also shown that an increase of $N_{\text{mag}}^{\text{supp}}$ generally improves the accuracy—with only very minor effects on the computational effort during the online evaluation of the surrogate model.

5.7 | Generalization to other material models

In principle, a CI surrogate can be set up for any material model with exclusive state-dependency. Gradient elasticity, where the energy density function also depends on the second order deformation gradient, $W = W(\mathbf{F}, \nabla_{\mathbf{x}}\mathbf{F})$, is a candidate that belongs to this category.³⁸ In such a case, the interpolation domain should be re-considered since the choice of the Hencky strain space was not made with higher gradients in mind.

Dissipative material laws might be covered or at least assisted by CI. For instance, standard viscoelastic material models³⁹ contain a hyperelastic term that can be directly treated by the CI method as in this article. History dependence might be treated by means of a decisive super-model switching between multiple CI schemes, each covering a certain region of the historic state space. However, the high dimensionality of this space would drastically increase the computational effort. To begin with, the numerical surrogate would be more complex. But even more severely, the state history would need to be tracked at each integration point on the current Scale N , as is the case in many classical dissipative material models involving internal variables. It could be an option for the super-model to decide to retreat to unreduced FE simulations on Scale $N - 1$ in case the state evolves along a path leaving the CI-covered domain.⁴⁰ Future works might reveal alternative pathways for the consideration of dissipative effects with notable contributions of CI for attaining computational efficiency.

ACKNOWLEDGEMENTS

This work is funded by the German Research Foundation (DFG)—project number 257987586, grant DFG FR2702/6 within the scope of the Emmy-Noether program. This work is funded by the German Research Foundation (DFG)—project number 406068690, grant DFG FR2702/8 within the scope of the Heisenberg program. This work is funded by the Deutsche Forschungsgemeinschaft (DFG, German Research Foundation) under Germany's Excellence Strategy—EXC-2075—project number 390740016.

CONFLICT OF INTEREST


The authors declare no potential conflict of interests.

AUTHOR CONTRIBUTIONS

O.K. and F.F. contributed to conceptualization and methodology. O.K. contributed to software, graphics, and writing. F.F. contributed to supervision, project administration, and funding acquisition.

ORCID

Oliver Kunc  <https://orcid.org/0000-0001-8437-9721>

Felix Fritzen  <https://orcid.org/0000-0003-4926-0068>

REFERENCES

- Voigt W. *Lehrbuch der Kristallphysik*. Berlin, Germany: Vieweg+Teubner Verlag; 1966.
- Ciarletta P, Izzo I, Micera S, Tendick F. Stiffening by fiber reinforcement in soft materials: a hyperelastic theory at large strains and its application. *J Mech Behav Biomed Mater*. 2011;4(7):1359-1368. <https://doi.org/10.1016/j.jmbbm.2011.05.006>.
- Kabel M, Böhlke T, Schneider M. Efficient fixed point and Newton–Krylov solvers for FFT-based homogenization of elasticity at large deformations. *Comput Mech*. 2014;54(6):1497-1514. <https://doi.org/10.1007/s00466-014-1071-8>.
- Rambausek M, Göküzüm FS, Nguyen LTK, Keip MA. A two-scale FE-FFT approach to nonlinear magneto-elasticity. *Int J Numer Methods Eng*. 2019;117(11):1117-1142. <https://doi.org/10.1002/nme.5993>.
- Yuan Z, Fish J. Multiple scale eigendeformation-based reduced order homogenization. *Comput Methods Appl Mech Eng*. 2009;198(21-26):2016-2038. <https://doi.org/10.1016/j.cma.2008.12.038>.
- Ramírez-Torres A, Penta R, Rodríguez-Ramos R, et al. Three scales asymptotic homogenization and its application to layered hierarchical hard tissues. *Int J Solids Struct*. 2018;130-131:190-198. <https://doi.org/10.1016/j.ijsolstr.2017.09.035>.
- Takano N, Okuno Y. Three-scale finite element analysis of heterogeneous media by asymptotic homogenization and mesh superposition methods. *Int J Solids Struct*. 2004;41(15):4121-4135. <https://doi.org/10.1016/j.ijsolstr.2004.02.049>.
- Nikolov S, Petrov M, Lymperakis L, et al. Revealing the design principles of high-performance biological composites using ab initio and multiscale simulations: the example of lobster cuticle. *Adv Mater*. 2010;22:519-526. <https://doi.org/10.1002/adma.200902019>.
- Wu M, Liu J, Lv X, Shi D, Zhu Z. A study on homogenization equations of fractal porous media. *J Geophys Eng*. 2018;15(6):2388-2398. <https://doi.org/10.1088/1742-2140/aac4c1>.
- Heida M, Kornhuber R, Podlesny J. Fractal homogenization of multiscale interface problems; 2017. arXiv preprint arXiv:1712.01172.
- Jarroudi ME, Er-Riani M. Homogenization of elastic materials containing self-similar rigid micro-inclusions. *Contin Mech Thermodyn*. 2018;31(2):457-474. <https://doi.org/10.1007/s00161-018-0700-4>.
- Kunc O, Fritzen F. Finite strain homogenization using a reduced basis and efficient sampling. *Math Comput Appl*. 2019;24(2). <https://www.mdpi.com/2297-8747/24/2/56#cite>.
- Pruchnicki E. Hyperelastic homogenized law for reinforced elastomer at finite strain with edge effects. *Acta Mech*. 1998;129(3):139-162. <https://doi.org/10.1007/BF01176742>.
- Nemat-Nasser S, Hori M. *Micromechanics: Overall Properties of Heterogeneous Materials*. 2nd ed. Amsterdam, Netherlands: Elsevier; 1999. <https://doi.org/10.1016/c2009-0-09128-4>.
- Bensoussan A, Lions JL, Papanicolaou G. *Asymptotic Analysis for Periodic Structures*. Amsterdam/New York: North-Holland; 1978. <https://doi.org/10.1090/chel/374>.
- Miehe C. Computational micro-to-macro transitions for discretized micro-structures of heterogeneous materials at finite strains based on the minimization of averaged incremental energy. *Comput Methods Appl Mech Eng*. 2003;192(5):559-591. [https://doi.org/10.1016/S0045-7825\(02\)00564-9](https://doi.org/10.1016/S0045-7825(02)00564-9).
- Feyel F. Multiscale FE² elastoviscoplastic analysis of composite structures. *Comput Mater Sci*. 1999;16(1-4):344-354. [https://doi.org/10.1016/S0927-0256\(99\)00077-4](https://doi.org/10.1016/S0927-0256(99)00077-4).
- Miehe C. Numerical computation of algorithmic (consistent) tangent moduli in large-strain computational inelasticity. *Comput Methods Appl Mech Eng*. 1996;134(3):223-240. [https://doi.org/10.1016/0045-7825\(96\)01019-5](https://doi.org/10.1016/0045-7825(96)01019-5).
- Kouznetsova V, Brekelmans WAM, Baaijens FPT. An approach to micro-macro modeling of heterogeneous materials. *Comput Mech*. 2001;27(1):37-48. <https://doi.org/10.1007/s004660000212>.

20. Kunc O, Fritzen F. Efficient assembly of linearized equations in nonlinear homogenization. *PAMM*. 2019;19(1). <https://doi.org/10.1002/pamm.201900322>.
21. Kunc O, Fritzen F. Generation of energy-minimizing point sets on spheres and their application in mesh-free interpolation and differentiation. *Adv Comput Math*. 2019;45(5-6):3021-3056. <https://doi.org/10.1007/s10444-019-09726-5>.
22. Fritzen F, Kunc O. Two-stage data-driven homogenization for nonlinear solids using a reduced order model. *Europ J Mech A/Solids*. 2018;69:201-220. <https://doi.org/10.1016/j.euromechsol.2017.11.007>.
23. Fritzen F, Kunc O. GitHub repository concentric interpolation; 2020. <https://github.com/EMMA-Group/ConcentricInterpolation>.
24. Fasshauer G, McCourt M. *Kernel-Based Approximation Methods Using Matlab*. 19th ed. Singapore: World Scientific; 2015. <https://doi.org/10.1142/9335>.
25. Fasshauer GE, Schumaker LL. Scattered data fitting on the sphere. *Math Methods Curves Surf II*. 1998;117-166.
26. Spahn J, Andrä H, Kabel M, Müller R. A multiscale approach for modeling progressive damage of composite materials using fast Fourier transforms. *Comput Methods Appl Mech Eng*. 2014;268:871-883. <https://doi.org/10.1016/j.cma.2013.10.017>.
27. Leuschner M, Fritzen F. Fourier-accelerated nodal solvers (FANS) for homogenization problems. *Comput Mech*. 2018;62(3):359-392. <https://doi.org/10.1007/s00466-017-1501-5>.
28. Rall LB, ed. *Automatic Differentiation: Techniques and Applications*. Berlin, Heidelberg/Germany: Springer; 1981. <https://doi.org/10.1007/3-540-10861-0>.
29. Fritzen F, Kunc O. GitHub repository MinimumEnergyPoints; 2020. <https://github.com/EMMA-Group/MinimumEnergyPoints>.
30. Yvonnet J, Monteiro E, He QC. Computational homogenization method and reduced database model for hyperelastic heterogeneous structures. *J Multiscale Comput Eng*. 2013;11(3):201-225. <https://doi.org/10.1615/IntJMultCompEng.2013005374>.
31. Brands B, Davydov D, Mergheim J, Steinmann P. Reduced-order modelling and homogenisation in magneto-mechanics: a numerical comparison of established hyper-reduction methods. *Math Comput Appl*. 2019;24(1). <https://doi.org/10.3390/mca24010020>.
32. Özdemir I, Brekelmans W, FE2 GM. computational homogenization for the thermo-mechanical analysis of heterogeneous solids. *Comput Methods Appl Mech Eng*. 2008;198(3-4):602-613. <https://doi.org/10.1016/j.cma.2008.09.008>.
33. Sirovich L. Turbulence and the dynamics of coherent structures. Part 1: coherent structures. *Q Appl Math*. 1987;45:561-571. <https://doi.org/10.1090/qam/910462>.
34. Yang Z, Long C, Sun Y. A high-order three-scale reduced asymptotic approach for thermo-mechanical problems of nonlinear heterogeneous materials with multiple spatial scales. *Europ J Mech A/Solids*. 2020;80:103905. <https://doi.org/10.1016/j.euromechsol.2019.103905>.
35. Kaliske M, Heinrich G. An extended tube-model for rubber elasticity: statistical-mechanical theory and finite element implementation. *Rubber Chem Technol*. 1999;72:602-632. <https://doi.org/10.5254/1.3538822>.
36. Doll S, Schweizerhof K. On the development of volumetric strain energy functions. *J Appl Mech*. 1999;67(1):17-21. <https://doi.org/10.1115/1.321146>.
37. Marckmann G, Verron E. Comparison of hyperelastic models for rubber-like materials. *Rubber Chem Technol*. 2006;79(5):835-858. <https://doi.org/10.5254/1.3547969>.
38. Forest S. Micromorphic approach for gradient elasticity, viscoplasticity, and damage. *J Eng Mech*. 2009;135(3):117-131. [https://doi.org/10.1061/\(asce\)0733-9399\(2009\)135:3\(117\)](https://doi.org/10.1061/(asce)0733-9399(2009)135:3(117)).
39. Simo J. On a fully three-dimensional finite-strain viscoelastic damage model: formulation and computational aspects. *Comput Methods Appl Mech Eng*. 1987;60(2):153-173. [https://doi.org/10.1016/0045-7825\(87\)90107-1](https://doi.org/10.1016/0045-7825(87)90107-1).
40. Fritzen F, Fernández M, Larsson F. On-the-fly adaptivity for nonlinear twoscale simulations using artificial neural networks and reduced order modeling. *Front Mater*. 2019;6(75):1-18. <https://doi.org/10.3389/fmats.2019.00075>.

How to cite this article: Kunc O, Fritzen F. Many-scale finite strain computational homogenization via Concentric Interpolation. *Int J Numer Methods Eng*. 2020;121:4689–4716. <https://doi.org/10.1002/nme.6454>